

Anatomy of the AGN in NGC 5548: II. The Spatial, Temporal and Physical Nature of the Outflow from HST/COS Observations

N. Arav¹, C. Chamberlain¹, G.A. Kriss^{2,3}, J.S. Kaastra^{4,5}, M. Cappi⁶, M. Mehdipour^{4,7}, P.-O. Petrucci^{8,9}, K.C. Steenbrugge^{10,11}, E. Behar¹², S. Bianchi¹³, R. Boissay¹⁴, G.Branduardi-Raymont⁷, E. Costantini⁴, J.C. Ely², J. Ebrero⁴, L. di Gesu⁴, F.A. Harrison¹⁵, S.Kaspi¹², J. Malzac^{16,17}, B. De Marco¹⁸, G. Matt¹³, K.P. Nandra¹⁸, S. Paltani¹⁴, B.M.Peterson^{19,20}, C. Pinto²¹, G. Ponti¹⁸, F. Pozo Nuñez²², A. De Rosa²³, H. Seta²⁴, F. Ursini^{8,9}, C.P.de Vries⁴, D.J.Walton¹⁵, and M. Whewell⁷

¹ Department of Physics, Virginia Tech, Blacksburg, VA 24061, USA.

² Space Telescope Science Institute, 3700 San Martin Drive, Baltimore, MD 21218, USA.

³ Department of Physics and Astronomy, The Johns Hopkins University, Baltimore, MD 21218, USA.

⁴ SRON Netherlands Institute for Space Research, Sorbonnelaan 2, 3584 CA Utrecht, the Netherlands.

⁵ Leiden Observatory, Leiden University, Post Office Box 9513, 2300 RA Leiden, Netherlands.

⁶ INAF-IASF Bologna, Via Gobetti 101, I-40129 Bologna, Italy.

⁷ Mullard Space Science Laboratory, University College London, Holmbury St. Mary, Dorking, Surrey, RH5 6NT, UK.

⁸ Univ. Grenoble Alpes, IPAG, F-38000 Grenoble, France.

⁹ CNRS, IPAG, F-38000 Grenoble, France.

¹⁰ Instituto de Astronomía, Universidad Católica del Norte, Avenida Angamos 0610, Casilla 1280, Antofagasta, Chile.

¹¹ Department of Physics, University of Oxford, Keble Road, Oxford, OX1 3RH, UK.

¹² Department of Physics, Technion-Israel Institute of Technology, 32000 Haifa, Israel.

¹³ Dipartimento di Matematica e Fisica, Università degli Studi Roma Tre, via della Vasca Navale 84, 00146 Roma, Italy.

¹⁴ Department of Astronomy, University of Geneva, 16 Ch. d'Ecogia, 1290 Versoix, Switzerland.

¹⁵ Cahill Center for Astronomy and Astrophysics, California Institute of Technology, Pasadena, CA 91125, USA.

¹⁶ Université de Toulouse, UPS-OMP, IRAP, Toulouse, France.

¹⁷ CNRS, IRAP, 9 Av. colonel Roche, BP 44346, 31028 Toulouse Cedex 4, France.

¹⁸ Max-Planck-Institut für extraterrestrische Physik, Giessenbachstrasse, D-85748 Garching, Germany.

¹⁹ Department of Astronomy, The Ohio State University, 140W 18th Avenue, Columbus, OH 43210, USA.

²⁰ Center for Cosmology & AstroParticle Physics, The Ohio State University, 191 West Woodruff Avenue, Columbus, OH 43210, USA.

²¹ Institute of Astronomy, University of Cambridge, Madingley Rd, Cambridge, CB3 0HA, UK.

²² Astronomisches Institut, Ruhr-Universität Bochum, Universitätsstraße 150, 44801, Bochum, Germany.

²³ INAF/IAPS - Via Fosso del Cavaliere 100, I-00133 Roma, Italy.

²⁴ Research Center for Measurement in Advanced Science, Faculty of Science, Rikkyo University 3-34-1 Nishi-Ikebukuro, Toshimaku, Tokyo, Japan.

October 9, 2018

ABSTRACT

Context. AGN outflows are thought to influence the evolution of their host galaxies and super massive black holes. Our deep multi-wavelength campaign on NGC 5548 revealed an unusually strong X-ray obscuration. The resulting dramatic decrease in incident ionizing flux on the outflow, allowed us to construct a comprehensive physical, spatial and temporal picture for the long-studied AGN wind in this object.

Aims. To determine the distance of the outflowing components from the central source; their total column density and the mechanism responsible for the observed absorption trough variability.

Methods. We study the UV spectra acquired during the campaign as well as from four previous epochs, where the outflows are detected as blue-shifted absorption troughs in the spectra of the object. Our principal analysis tools are ionic column density extraction techniques, photoionization models based on the code CLOUDY, and collisional excitation simulations.

Results. A simple model based on a fixed total column-density absorber, reacting to changes in ionizing illumination, matches the very different ionization states seen in five spectroscopic epochs spanning 16 years. The main outflow component is situated at 3.5 ± 1 pc from the central source. Three other components are situated between 5-70 pc and two are further than 100 pc. The wealth of observational constraints and the disparate relationship of the observed X-ray and UV flux between different epochs make our physical model a leading contender for interpreting trough variability data of quasar outflows.

Conclusions. This campaign, in combination with prior data, yields the first simple model that can explain the physical characteristics and the substantial variability observed in an AGN outflow.

Key words. galaxies: Seyfert – galaxies: active – X-rays: galaxies

1. Introduction

AGN outflows are detected as blueshifted absorption troughs, with respect to the object systemic redshift. Such outflows in powerful quasars can expel sufficient gas from their host galaxies to halt star formation, limit their growth and lead to the co-evolution of the size of the host and the mass of its central super massive black holes (e.g., Ostriker et al. 2010; Hopkins & Elvis 2010; Soker & Meiron 2011; Ciotti et al. 2010; Faucher-Giguère et al. 2012; Borguet et al. 2013; Arav et al. 2013). Therefore, deciphering the properties of AGN outflows is crucial for testing their role in galaxy evolution.

Nearby bright AGN are excellent laboratories for studying these outflows as they yield: a) high-resolution UV data, which allow us to study the outflow kinematics and can yield diagnostics for their distance from the central source; and b) high quality X-ray spectra that give the physical conditions for the bulk of the outflowing material (e.g., Steenbrugge et al. 2005; Gabel et al. 2005; Arav et al. 2007; Costantini et al. 2007; Kaastra et al. 2012). Thus, such observations are a vital stepping stone for quantifying outflows from the luminous (but distant) quasars, for which high quality X-ray data are not available.

For these reasons, we embarked on a deep multiwavelength campaign on the prototypical AGN outflow seen in the intensively studied Seyfert 1 galaxy NGC 5548. For the past 16 years, this outflow has shown 6 kinematic components in the UV band (labeled in descending order of velocity, following Crenshaw et al. 2003), and their associated X-ray warm absorber (WA). Our 2013 campaign revealed a new X-ray obscurer accompanied by broad UV absorption (analyzed in Kaastra et al. 2014). The appearance of the obscurer allows us to derive a comprehensive physical picture of the long-term observed outflow, which we report here.

The plan of the paper is as follows: In § 2 we describe the observations and data reduction; in § 3 we analyze the key component of the outflow; in § 4 we discuss the remaining 5 components; in § 5 we connect the results of the UV analysis with those of the X-ray warm absorber of the same outflow; and in § 6 we compare our results with previous studies, discuss the implication of our results to the variability of AGN outflow troughs in general, and elaborate on the connection between the X-ray obscurer and the persisting outflow; In § 7 we summarize our results.

2. Observations and Data Reduction

Our 2013 multiwavelength campaign on NGC 5548 included coordinated observations using XMM-Newton, HST, Swift, INTEGRAL, and NuSTAR. Kaastra et al. (2014) describe the overall structure of the campaign. A full log of all the observations is given by Mehdipour et al (2014). Here we present a more detailed analysis of the UV observations we obtained using the Cosmic Origins Spectrograph (COS) (Green et al. 2012) on-board *HST*. We obtained five COS observations simultaneously with five of the XMM-Newton observations between 2013-06-22 and 2013-08-01. Each two-orbit observation used gratings G130M and G160M at multiple central wavelength settings and multiple focal-plane positions (FP-POS) to cover the wavelength range from 1132 Å to 1801 Å at a resolving power of $\sim 15,000$. Table A.1 lists the observation dates of the individual visits, the exposure times, and the continuum flux measured at 1350 Å in the rest frame, as well as corresponding information for archival

HST observations of NGC 5548 that are also used in this analysis. The five observations from the summer of 2013 were optimally weighted to produce an average spectrum that we use for our analysis. Kaastra et al. (2014) describe the data reduction process from the calibration of the data to the production of this average spectrum.

The 2013 average HST/COS spectrum with all identified absorption features is shown in Figure A1. As described in Kaastra et al. (2014), we modeled the emission from NGC 5548 using a reddened power law (with extinction fixed at $E(B - V) = 0.02$, Schlegel et al. 1998), weak Fe II emission longward of 1550 Å in the rest frame, broad and narrow emission lines modeled with several Gaussian components, blue-shifted broad absorption on all permitted transitions in NGC 5548, and a Galactic damped Ly α absorption line. Using this emission model, we normalized the average spectrum to facilitate our analysis of the narrow intrinsic absorption lines in NGC 5548. Figure 1 shows normalized spectra for absorption lines produced by Si III $\lambda 1206$, Si IV $\lambda 1394, 1403$, C IV $\lambda 1548, 1550$, N V $\lambda 1238, 1242$, and Ly α as a function of rest-frame velocity relative to a systemic redshift of $z = 0.017175$ (de Vaucouleurs et al. 1991) via the NASA/IPAC Extragalactic Database (NED).

As shown in Table A.1, high-resolution UV spectra of NGC 5548 using HST cover an additional four epochs stretching back to 1998. We use the calibrated data sets for each of these observations as obtained from the Mikulski Archive for Space Telescopes (MAST) at the Space Telescope Science Institute (STScI). We compare the strengths of the narrow UV absorption troughs for each of these epochs with our new data set from 2013 in Figs. A2 and A3.

3. Physical and temporal characteristics of Component 1

The key for building a coherent picture of the long-seen outflow is component 1: the strongest and highest velocity outflow component (centered at -1160 km s^{-1}). Due to the strong suppression of incident ionizing flux by the obscurer, the 2013 HST/COS data of component 1 show a wealth of absorption troughs from ions never before observed in the NGC 5548 outflow. These data allow us to decipher the physical characteristics of this component. In § 3.1 we use the column density measurements of P V, P III, Fe III, and Si II as input in photoionization models, and derive the total hydrogen column density for component 1 of $\log(N_H) = 21.5^{+0.4}_{-0.2} \text{ cm}^{-2}$, and an ionization parameter of $\log(U_H) = -1.5^{+0.4}_{-0.2}$. In § 3.2 we use the column density measurements of C III* and Si III* to infer the electron number density $\log(n_e) = 4.8 \pm 0.1 \text{ cm}^{-3}$, which combined with the value of the incident U_H yields a distance $R = 3.5 \pm 1$ parsec between component 1 and the central source. In § 3.3 we construct a simple model based on a fixed total column-density absorber, reacting to changes in ionizing illumination, that matches the very different ionization states seen in five HST high-resolution spectroscopic epochs spanning 16 years.

3.1. Total Column Density (N_H) and Ionization Parameter (U_H)

In the Appendix we describe the methods we use to derive the ionic column densities (N_{ion}) from the outflow absorption troughs. Table 2 gives the N_{ion} measurements for all observed troughs of all 6 outflow components in the 5 HST epochs (spanning 16 years) of high-resolution UV spectroscopy. The upper

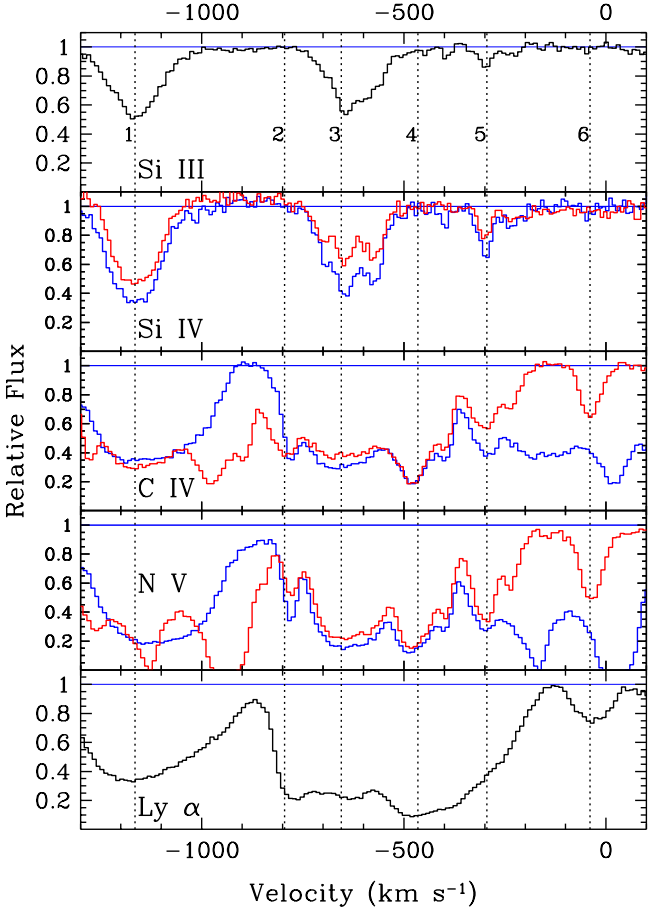


Fig. 1. Intrinsic absorption features in the 2013 COS spectrum of NGC 5548. Normalized relative fluxes are plotted as a function of velocity relative to the systemic redshift of $z = 0.017175$, top to bottom: Si III $\lambda 1206$, Si IV $\lambda 1394, 1403$, C IV $\lambda 1548, 1550$, N V $\lambda 1238, 1242$, and Ly α , as a function of rest-frame velocity. For the doublets the red and blue components are shown in red and blue, respectively. Dotted vertical lines indicate the velocities of the absorption components numbered as in Crenshaw et al. (2003).

and lower limits were derived using the Apparent Optical Depth (AOD) method. All the reported measurements were done using the Partial Covering (PC) method. We used the Power-Law (PL) method only on the C III* in order to quantify the systematic error due to different measuring methods (see § 3.2 and Fig. 4).

The N_{ion} we measure are a result of the ionization structure of the outflowing material, and can be compared to photoionization models to determine the physical characteristics of the absorbing gas. As boundary conditions for the photoionization models, we need to specify the choice of incident Spectral Energy Distribution (SED), and the chemical abundances of the outflowing gas.

We make the simple (and probably over-restrictive) assumption that the shape of the SED emitted from the accretion disk did not change over the 16 years of high-resolution UV spectroscopy. Specifically, we assume that the emitted SED has the same shape it had when we obtained simultaneous X-ray/UV observations in 2002 (the “high” SED in Figure 2, determined by Steenbrugge et al. 2005). In 2013 the obscurer absorbed much of the soft ionizing photon flux from this SED before it reached component 1. We model the incident SED on component 1 as

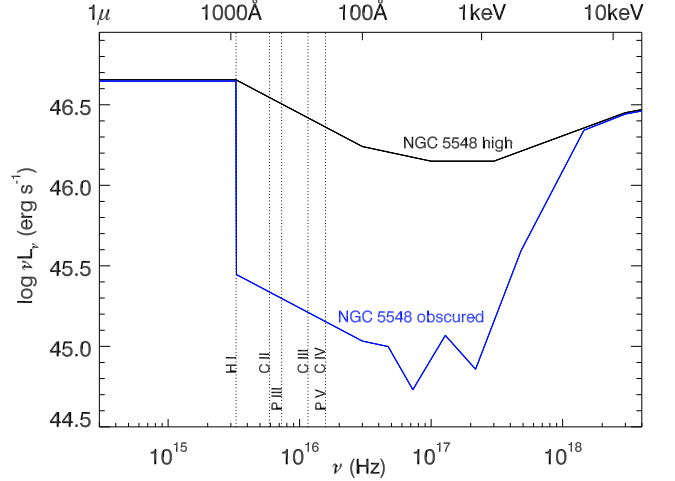


Fig. 2. The adopted NGC 5548 SEDs. In black we show the SED for NGC 5548 in 2002 at an unobscured X-ray flux (hereafter “high SED,” from Steenbrugge et al. 2005). In blue we show the SED appropriate to the 2013 epoch, where for the same flux at 1000 Å, the new X-ray obscurer reduced the ionizing flux by a factor of 17 between 1 Ry and 1 keV (obscured SED). The ionization potentials for destruction of some of the prominent observed species are shown by the vertical lines.

the “obscured” SED in Figure 2, and further justify its specific shape in § 3.3. For abundances, we use pure proto-Solar abundances given by Lodders et al. (2009).

With the choice of SED and chemical abundances, two main parameters govern the photoionization structure of the absorber: the total hydrogen column density (N_H) and the ionization parameter

$$U_H \equiv \frac{Q_H}{4\pi R^2 n_H c} \quad (1)$$

where Q_H is the rate of hydrogen-ionizing photons emitted by the object, c is the speed of light, R is the distance from the central source to the absorber and n_H is the total hydrogen number density. We model the photoionization structure and predict the resulting ionic column densities by self-consistently solving the ionization and thermal balance equations with version 13.01 of the spectral synthesis code CLOUDY, last described in Ferland et al. (2013). We assume a plane-parallel geometry for a gas of constant n_H .

To find the pair of (U_H, N_H) that best predicts the set of observed column densities, we vary U_H and N_H in 0.1 dex steps to generate a grid of models (following the same approach described in Borguet et al. 2012b) and perform a minimization of the function

$$\chi^2 = \sum_i \left(\frac{\log(N_{i,mod}) - \log(N_{i,obs})}{\log(N_{i,obs}) - \log(N_{i,obs} \pm \sigma_i)} \right)^2 \quad (2)$$

where, for ion i , $N_{i,obs}$ and $N_{i,mod}$ are the observed and modeled column densities, respectively, and σ_i is the error in the observed column density. The measurement errors are not symmetric. We use the positive error ($+\sigma_i$) when $\log(N_{i,mod}) > \log(N_{i,obs})$ and the negative error ($-\sigma_i$) when $\log(N_{i,mod}) < \log(N_{i,obs})$.

The ionization solution for component 1 at the 2013 epoch is shown in figure 3. We only show constraints from N_{ion} measurements, and note that all the lower limits reported in Table 2 are

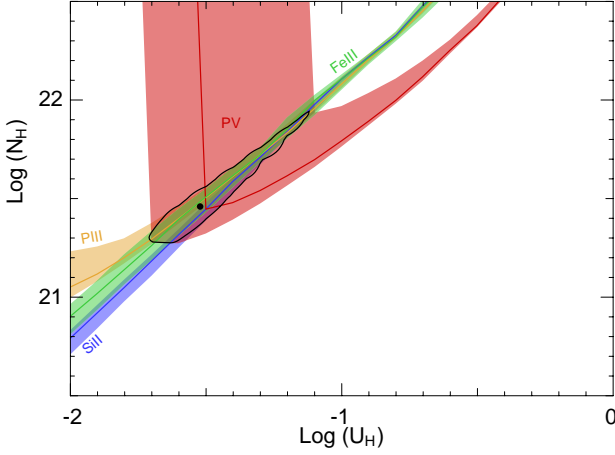


Fig. 3. A photoionization phase plot showing the ionization solution for component 1 epoch 2013. We use the obscured SED and assumed proto-solar metallicity (Lodders et al. 2009). Solid lines and associated colored bands represent the locus of U_H , N_H models, which predict the measured N_{ion} , and their 1σ uncertainties. The black dot is the best solution and is surrounded by a $1\sigma \chi^2$ contour.

satisfied by this solution. We find $\log(N_H) = 21.5^{+0.4}_{-0.2} \text{ cm}^{-2}$, and an ionization parameter of $\log(U_H) = -1.5^{+0.4}_{-0.2}$, where the errors are strongly correlated as illustrated by the $1\sigma \chi^2$ contour.

3.2. Number Density and Distance

As shown in Figure 4, we detect absorption troughs from the C III^* 1175 Å multiplet, arising from the metastable $3P_j$ levels of the $2s2p$ term. As detailed in Gabel et al. (2005), the excited C III^* 1175 Å multiplet comprises six lines arising from three J levels. The J=0 and J=2 levels have significantly lower radiative transition probabilities to the ground state than the J=1 level and are thus populated at much lower densities than the latter. In particular, figure 5 in Borguet et al. (2012a) shows that the relative populations of the three levels are a sensitive probe to a wide range of n_e while being insensitive to temperature. The two high-S/N troughs from the J=2 level allow us to accurately account for the mild saturation in these troughs and therefore to derive reliable N_{ion} for both levels. From these measurements we infer $\log(n_e) = 4.8 \pm 0.1 \text{ cm}^{-3}$ (see Fig. 4). We also detect two shallow troughs from the same metastable level of Si III^* (see panel b of Fig. 4), which we use to measure an independent and consistent value for n_e (see panel c of Fig. 4). The collisional excitation simulations shown in Figure 4c were performed using version 7.1.3 of CHIANTI (Dere et al. 1997; Landi et al. 2013), with a temperature of 10,000K (similar to the predicted temperature of our CLOUDY model for component 1 during the 2013 epoch).

In addition to the C III^* and Si III^* troughs, the 2013 COS spectra of component 1 show several additional troughs from excited states: C II^* , Si II^* , P III^* , S III^* and Fe III^* (as well as their associated resonance transitions). Careful measurement of those troughs show that in these cases, the deduced n_e is a lower limit that is larger than the critical density of the involved excited and zero energy levels. In all cases the critical densities are below

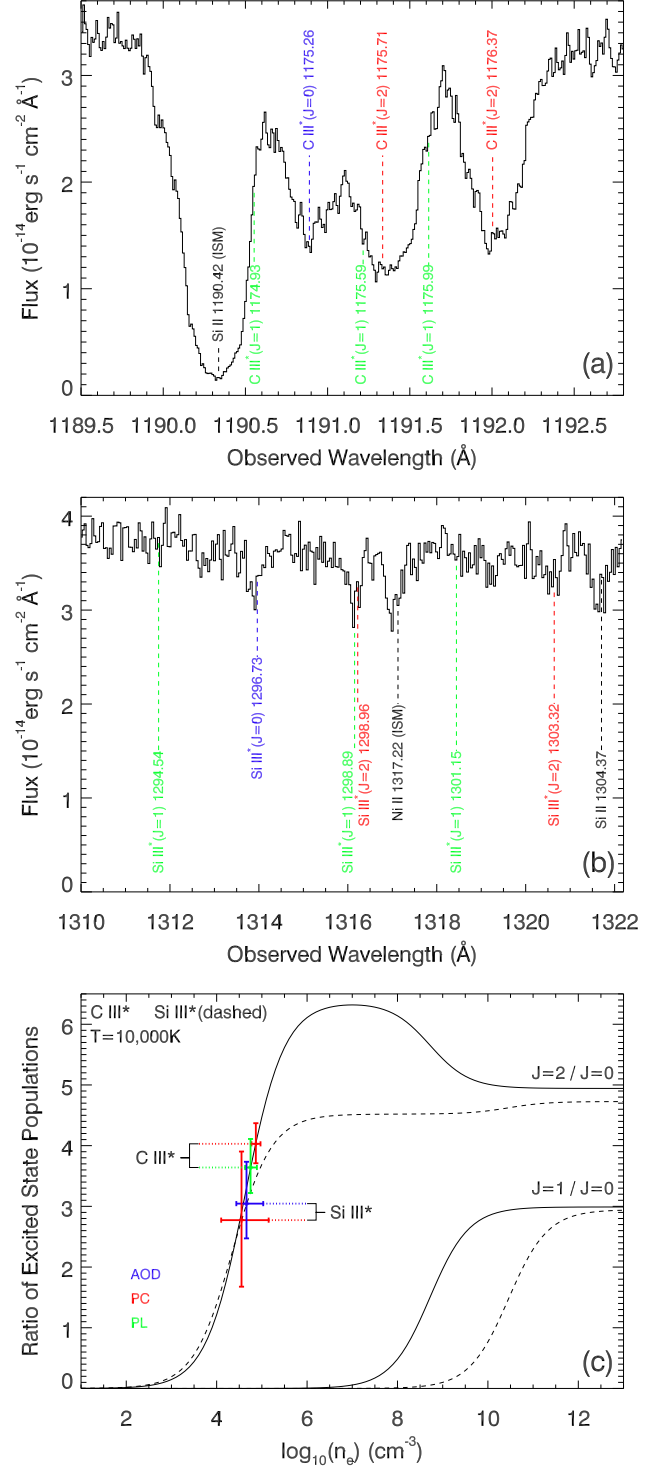


Fig. 4. **a)** Absorption spectrum for the C III^* 1175 Å multiplet. The 2013 COS spectrum shows clear and relatively unblended individual troughs from the J=2 and J=0 levels, but no contribution from the J=1 level that is populated at higher densities (see panel c). **b)** Absorption spectrum for the Si III^* 1298 Å multiplet (similar in level structure to the C III^* 1175 Å multiplet). The 2013 COS spectrum shows shallow but highly significant individual troughs from the J=2 and J=0 levels, but again no contribution from the J=1 level that is populated at higher densities. **c)** C III^* and Si III^* level population ratios, theory and measurements. The computed populations for the J=2/J=0 and J=1/J=0 are plotted as a function of electron number density for both ions (see text for elaboration). The crosses show the measured ratios for the J=2/J=0 ratio of both ions. From the C III^* ratios we infer $\log(n_e) = 4.8 \pm 0.1 \text{ cm}^{-3}$, where the error includes both statistical and systematic effects. This value is fully consistent with the one inferred from the Si III^* ratio, where in the case of Si III^* the statistical error is larger since the troughs are much shallower.

$\log(n_e) = 4.8 \text{ cm}^{-3}$, thus they are consistent with the n_e measurement we derive from the C III* and Si III* troughs.

As can be seen from the definition of the ionization parameter U_H (Equation 1), knowledge of the hydrogen number density n_H for a given U_H and N_H allows us to derive the distance R . Our photoionization models show that for component 1, $\log(U_H) = -1.5$ and since $n_e \approx 1.2n_H$ (as is the case for highly ionized plasma), $n_H = 5.3 \times 10^4 \text{ cm}^{-3}$. To determine the Q_H that affects component 1, we first calculate the bolometric luminosity using the average flux at 1350 \AA for visits 1-5 in 2013, the redshift of the object and the obscured SED (see Fig. 2). We find $L_{bol} = 2.6 \times 10^{44} \text{ erg s}^{-1}$ and from it, $Q_H = 6.9 \times 10^{52} \text{ s}^{-1}$. Therefore, equation (1) yields $R = 3.5^{+1.0}_{-1.2} \text{ pc}$, where the error is determined from propagating the errors of the contributing quantities.

Assuming the canonical 50% global covering factor for Seyfert outflows (Crenshaw et al. 1999), and using equation (1) in Arav et al. (2013) we find that the mass flux associated with the UV manifestation of component 1 is $1.0^{+2.0}_{-0.5}$ solar masses per year, and that the kinetic luminosity is $4^{+8}_{-2} \times 10^{41} \text{ erg s}^{-1}$. We note that most of the N_H in the various outflow components is associated with the higher ionization X-ray phase of the outflow. Therefore, we defer a full discussion of the total mass flux and kinetic luminosity of the outflow to a future paper that will present a combined analysis of the UV and X-ray data sets.

3.3. Modeling the Temporal Behavior of the Outflow

The absorption troughs of component 1 change drastically between the five HST high-resolution spectroscopic epochs spanning 16 years (see figures A2 and A3). After finding the location and physical characteristics of component 1 using the 2013 data, the next step is to derive a self-consistent temporal picture for this component. There are two general models that explain trough variability in AGN outflows (e.g., Barlow et al. 1992; Gabel et al. 2003; Capellupo et al. 2012; Arav et al. 2012; Filiz Ak et al. 2013, and references therein). One model attributes the trough variability to changes of the ionizing flux experienced by the outflowing gas. In its simplest form, this model assumes that the total N_H along the line of sight does not change as a function of time. A second model invokes material moving across the line of sight, which in general causes changes of N_H along the line of sight as a function of time to explain the observed trough changes.

In the case of component 1, we have enough constraints to exclude the model of material moving across our line of sight. The outflow is situated at 3.5 pc from the central source, which combined with the estimated mass of the black hole in NGC 5548 (4×10^7 solar masses; Pancoast et al. 2013), yields a Keplerian speed of $1.9 \times 10^7 \text{ cm s}^{-1}$ at that distance. As can be seen from figure A1, 2/3 of the emission at the wavelength of component 1 arises from the C IV Broad Emission Line (BEL). Therefore, the transverse motion model crucially depends on the ability of gas clouds to cross most of the projected size of the Broad Line Region (BLR) in the time spanning the observations epochs. Reverberation studies (Korista et al. 1995) give the diameter of the C IV BLR as 15 light days or $3.9 \times 10^{16} \text{ cm}$, which for $v_{\perp} = 1.9 \times 10^7 \text{ cm s}^{-1}$, yields a crossing time of 2.0×10^9 seconds, or 65 years.

Thus, in the 16 years between our epochs, material that moves at the Keplerian velocity, 3.5 pc away from the NGC 5548 black hole, will cross only about 25% of the projected size of the C IV BLR. Therefore, the much larger change in the resid-

ual intensity of the component 1 C IV trough cannot be attributed to new material appearing due to transverse motion at this distance. We note that 25% motion across the projected size of the C IV BLR is a highly conservative limit for two reasons: 1) at certain velocities there are changes of 50% in the residual intensity in the component 1 C IV trough between the 2011 and 2013 epochs; and in the elapsing 2 years, transverse motion will only cover 3% of the projected size of the C IV BLR; 2) material that moves away from the central source under the influence of radial forces should conserve its angular momentum. Therefore, if it moved to distances that are much larger compared with its initial distance, its $v_{\perp} \ll v_{kep}$ at its current distance. We conclude that even under favorable conditions, the transverse motion model of gas into or out of the line of sight cannot explain the observed behavior of component 1 over the 5 observed epochs.

Can changes of the ionizing flux experienced by the outflowing gas explain the observed trough changes? We construct such a model under the simplest and restrictive assumption that the N_H of component 1 did not change over the 16 years spanning the 5 high resolution UV spectral epochs. Furthermore, for $\log(n_e) = 4.8 \text{ (cm}^{-3}\text{)}$, the absorber should react to changes in incident ionizing flux on time-scales of 5 days (see eq. 3 here, and discussion in Arav et al. 2012). Therefore, for component 1 we use the restrictive assumption of a simple photoionization equilibrium, determined by the flux level of the specific observation.

In 1998 the AGN was in a high flux level of $F=6$ (measured at 1350 \AA rest-frame and given in units of $10^{-14} \text{ ergs s}^{-1} \text{ cm}^{-2} \text{ \AA}^{-1}$). At that epoch the absorber only showed a Ly α trough necessitating $\log(U_H) \gtrsim 0.1$ (otherwise a N V trough would be detected, see Fig. 5). In 2002 the AGN was in a medium flux level with $F=2$, at which time the absorber showed C IV and N V troughs in addition to Ly α . In 2004 the AGN was at a historically low flux of $F=0.25$. In that epoch a Si III trough appeared in addition to the C IV, N V and Ly α troughs; however, a C II trough did not appear. The combination of the Si III and C II constraints necessitates $-1.3 < \log(U_H) < -1.15$ (see Fig. 5). The change in $\log(U_H)$ required by the photoionization models agrees remarkably well with the change in flux between the 1998 and 2004 epochs as $\log(F_{2004}/F_{1998}) = -1.4$. Thus, a constant N_H absorber yields an excellent fit for the absorption features from two epochs with the same spectral energy distribution (high SED in Figure Fig. 5), but with very different U_H values. Comparison of several key troughs between the 5 epochs is shown in Figs. A2 and A3. The 1350 \AA flux measurements, plus observation details are given in Table A.1 and the derived column densities for all the outflow features are given in Table A.2.

In 2013 the AGN flux was $F=3$. With this flux level and assuming the same SED, the U_H value should have been 50% higher than in 2002, and we would expect to see only C IV, N V and Ly α troughs. Instead we also detect Si III, C II, Si II and Al II. Therefore, the incident SED for component 1 must have changed, and indeed the 2013 soft X-ray flux is 25 times lower compared to that of the 2002 epoch (see Fig. 1 in Kaastra et al. 2014). This drop is caused by the newly observed obscurer close to the AGN, which does not fully cover the source (Kaastra et al. 2014). We found a good match to the UV absorption and soft X-ray flux with an SED that is similar to that of the high flux one longward of 1 Ry, but abruptly drops to 6% of that flux between 1 Ry and 1 keV (see Fig. 2). This picture is consistent with the transmitted flux resulting from the low-ionization, partial covering model of the obscurer derived in Kaastra et al. (2014). To complete the UV picture for component 1, in 2011 NGC 5548 showed $F=6$, equal to that of the 1998 epoch. However, C IV

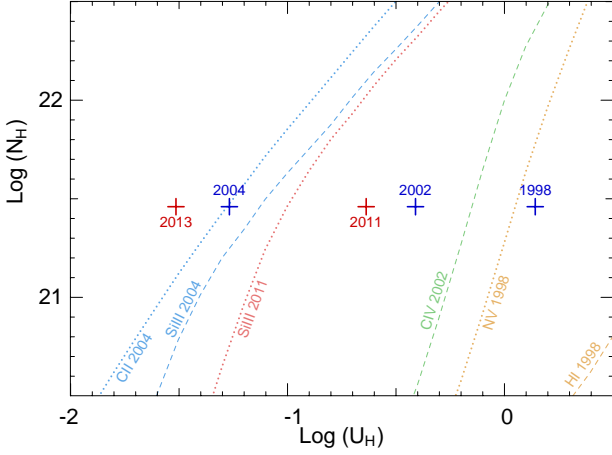


Fig. 5. A photoionization phase plot showing the ionization solutions for component 1 for all 5 epochs. The 2013 epoch solution is identical to the one shown in Fig. 3. For the 1998, 2002, and 2004 epochs we used the high SED (see Fig. 2) with the same abundances, and their ionization solutions are shown in blue crosses. Dashed lines represent N_{ion} lower-limit that allow the phase-space above the line, while the dotted lines are upper-limits that allow the phase-space below the line (only the most restrictive constraints are shown). N_H is fixed for all epochs at the value determined from the 2013 solution. For 1998, 2002 and 2004 the difference in U_H values is determined by the ratio of fluxes at 1350\AA and the actual value is anchored by the observed N_{ion} constraints. As explained in § 3.3, the U_H position of the 2011 epoch is less tightly constrained. The solution for each epoch satisfies all the N_{ion} constraints for that epoch.

and N v are clearly seen in the 2011 epoch but not any of the other ionic species seen in 2013. To explain this situation we assume that the obscurer was present at the 2011 epoch, but it only blocked somewhere between 50–90% of the emitted ionizing radiation between 1 Ry and 1 keV. The possible presence of a weaker X-ray obscurer is also suggested by broad absorption on the blue wing of the C IV emission line in 2011 that is weaker than that seen in 2013.

To summarize, a simple model based on a fixed total column-density absorber, reacting to changes in ionizing illumination, matches the very different phenomenology seen in all high-resolution UV spectra of component 1 spanning 16 years. Figure 7 gives a schematic illustration of the temporal model.

4. Components 2-6

What are the distances and physical conditions (N_H and U_H) for the other 5 outflow components (2-6)? As we show below, we can derive distances (or interesting limits of) for all these UV components and some loose constraints on the N_H and U_H of components 3 and 5. Figure 7 gives the velocities and distances of all 6 components, as well as a schematic illustration for their temporal behavior.

Constraining the Distances: components 2-6 do not show absorption from excited levels (Except for component 3, whose C II/C II* troughs only yield a lower limit for n_e). However, components 3 and 5 show clear variations in their Si III and Si IV troughs between our 2013/6/22 and 2013/8/1 observations, but

not between the 2013/7/24 and 2013/8/1 ones, when we do see changes in component 1. Using the formalism given in § 4 of Arav et al. (2012), we can deduce the n_e of these components from the observed time lags. Suppose an absorber in photoionization equilibrium experiences a sudden change in the incident ionizing flux such that $I_i(t > 0) = (1 + f)I_i(t = 0)$, where $-1 \leq f \leq \infty$. Then the timescale for change in the ionic fraction is given by:

$$t^* = \left[-f\alpha_i n_e \left(\frac{n_{i+1}}{n_i} - \frac{\alpha_{i-1}}{\alpha_i} \right) \right]^{-1}, \quad (3)$$

where α_i is the recombination rate of ion i and n_i is the fraction of a given element in ionization stage i . From the 40 days that separate epochs showing trough changes and the 7 days separating epochs with no change, we can deduce $3.5 < \log(n_e) < 4.5$ (cm^{-3}) for both components, otherwise their troughs would not react to changes in incident ionizing flux in the observed way, despite the large changes in incident ionizing flux over that period. Assuming a similar U_H to that of component 1 (see discussion below), this n_e range yields distances of $5 < R < 15$ parsec. Similarly, component 6 shows C IV and N v troughs in 2011 but not in 2002. This nine years timescale yields $R < 100$ parsec. Component 2 and component 4 do not show changes in the UV absorption between any of the epochs. Therefore, we can derive a lower limit for their distance of $R > 130$ parsec.

Constraining N_H and U_H : It is not feasible to put physically interesting constraints on components 2, 4 and 6. First, they only show troughs from C IV, N v, and Ly α , which (based on our analysis of component 1) are probably highly saturated. Second, the ionization time-scales of components 2 and 4 are larger than 16 years. Therefore, even if a U_H can be deduced from the measurements, it will only be a representative average value for a period of time larger than 16 years.

Figure 6 shows the N_H – U_H phase plot for component 3 based on the N_{ion} reported in Table A.2 (the Ly α and C IV N_{ion} lower limits are trivially satisfied by the lower limit shown for the N v N_{ion}). The phase plot constraints given by the N_{ion} measurements are mostly parallel to each other. Therefore, the N_H – U_H constraints are rather loose, allowing a narrow strip from $\log(N_H) = 19.6$ and $\log(U_H) = -2$, to $\log(N_H) = 21.5$ and $\log(U_H) = -1.1$. If we take the most probable value of $\log(U_H) = -1.3$, the distance estimate for component 3 will drop by 30% compared with the estimate of $5 < R < 15$ parsec, which used the $\log(U_H) = -1.5$ of component 1. For component 5, the situation is rather similar, as the detected Si III and Si IV allow a narrow strip from $\log(N_H) = 19.2$ and $\log(U_H) = -1.8$, to $\log(N_H) = 20.7$ and $\log(U_H) = -1.2$, while the lowest χ^2 is achieved at $\log(N_H) = 20.7$ and $\log(U_H) = -1.3$.

5. Comparison with the Warm Absorber Analysis

How do the physical characteristics inferred from the outflows' UV diagnostics compare to the properties of the X-ray manifestation of the outflow known as the Warm Absorber? Since the soft X-ray flux in our 2013 data is very low due to the appearance of the obscurer, we cannot characterize the WA that is connected with the 6 UV outflow components at that epoch. Our main inferences about the WA are from the 2002 epoch when we obtained simultaneous X-ray and UV spectra of the outflow (when no obscurer was present) that gave a much higher soft X-ray flux (compared with the 2013 observations) and allowed a detail modeling of the WA in that epoch (Steenbrugge et al. 2005; Kaastra et al. 2014). Due to the inherent complications

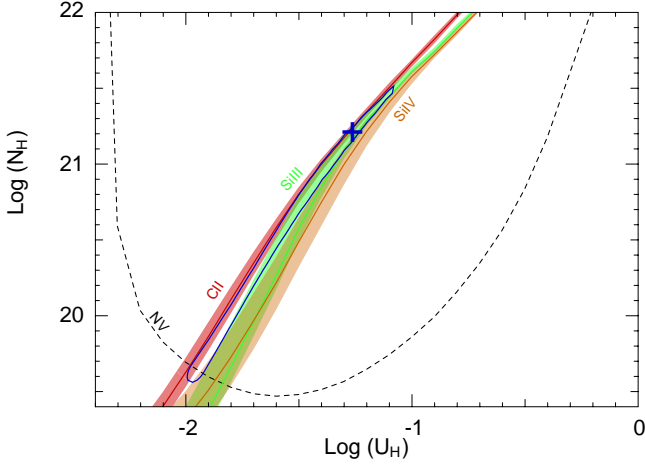


Fig. 6. A photoionization phase plot showing the ionization solution for component 3 epoch 2013. As for component 1, we use the obscured SED and assumed proto-solar metallicity (Lodders et al. 2009). Solid lines and associated colored bands represent the locus of U_H, N_H models, which predict the measured N_{ion} , and their 1σ uncertainties, while the dashed line is the lower limit on the N v column density that permits the phase-space above it. The blue cross is the best χ^2 solution and is surrounded by a 1σ χ^2 blue contour.

of comparing analyses on different spectral regions (X-ray and UV) separated by 11 years (2002 and 2013), of a clearly time-dependent phenomenon, we defer a full comparison to a later paper (Ebrero et al 2015). Here we outline some of the main points in such a comparison, based on the analysis presented here and the published analysis of the WA (Steenbrugge et al. 2005; Kaastra et al. 2014) and discuss some of the similarities and challenges of such a combined analysis.

1. Kinematic Similarity. There is kinematic correspondence between the UV absorption troughs in components 1–5 and the six ionization components (A–F) of the X-ray WA (Kaastra et al. 2014, see Table 1 here). X-ray components F and C span the width of UV component 1. X-ray component E matches UV component 2. The lowest ionization X-ray components, A and B comprise the full width of the blended UV troughs of components 3 and 4. Finally, X-ray component D kinematically matches UV component 5. However, as we show in point 2 below, this kinematic matching is physically problematic as the ionization parameters of WA components C, D, E and F are too high to produce observed troughs from C iv and N v that are observed in all the UV components.

2. Comparing similar ionization phases.

We note that the X-ray analysis of the WA in the Chandra 2002 observations uses a different ionization parameter (ξ) than the U_H we use here; where $\xi \equiv L/(n_H r^2)$ (erg cm) with n_H being the hydrogen number density, L the ionizing luminosity between 13.6 eV and 13.6 keV and r the distance from the central source. For the high SED, $\log(U_H) = \log(\xi) + 1.6$. In Table 1, we give the $\log(U_H)$ for the WA components. From the WA analysis and figure 5 here, we deduce that 90% of the WA material (components C, D, E and F in Table S2 of Kaastra et al. 2014) is in too high an ionization stage to produce measurable lines from the UV observed ions (e.g., C iv, N v). Only component A and B of

Table 1. Comparison between the UV and WA components

Component	Velocity ^a (km s ⁻¹)	$\log(N_H)$ (cm ⁻²)	$\log(U_H)$ (2002)
UV 1 ^b	-1160	$21.5^{+0.4}_{-0.2}$	$-0.4^{+0.4}_{-0.2}$
UV 2	-720	—	—
UV 3	-640	19.6 – 21.5	(-0.9) – 0.0
UV 4	-475	—	—
UV 5	-300	19.2 – 20.7	(-0.7) – (-0.1)
UV 6	-40	—	—
WA A ^c	-588 ± 34	20.30 ± 0.12	-0.82 ± 0.08
WA B	-547 ± 31	20.85 ± 0.06	-0.09 ± 0.05
WA C	-1148 ± 20	21.18 ± 0.08	0.55 ± 0.03
WA D	-255 ± 25	21.03 ± 0.07	0.76 ± 0.03
WA E	-792 ± 25	21.45 ± 0.12	1.34 ± 0.08
WA F	-1221 ± 25	21.76 ± 0.13	1.53 ± 0.05

^avelocity centroid of the component

^bUV components 1-6 are arranged by decreasing absolute velocity.

^cParameters for Warm Absorber components A-F are from Table S2 of Kaastra et al. (2014). They are arranged by increasing ionization parameter.

the WA are at low enough ionization states to give rise to the UV observed material.

3. Assuming constant N_H for the UV components and components A and B of the WA.

Our temporal model for component 1 has a constant N_H value in all the observed epochs, including 2002. The model also predicts the U_H of the 2002 epoch (see Fig. 5). We can therefore compare the predictions of this model to the results of the re-analysis of the 2002 WA (Kaastra et al. 2014), provided that the N_H for components A and B of the WA also did not change over the 11 years between the epochs. We note that since UV component 1 is the closest to the central source, the assumption of constant N_H for the other UV components, over this 11 years time period, is reasonable (see discussion in § 3.3). Therefore, we use the same ionization assumptions for UV components 3 and 5 as for component 1. That is, their N_H is fixed to the 2013 value and their $\log(U_H)_{2002} = \log(U_H)_{2013} + 1.1$, which are the values we list in Table 1. We do not have empirical constraints on the distances of WA components A-F from the central source.

4. Comparing UV components 1 and 3 to components A and B of the WA.

Using proto-Solar abundances (Lodders et al. 2009), our 2002 model prediction for UV component 1 has $\log(N_H) = 21.5^{+0.4}_{-0.2}$ cm⁻², and an ionization parameter of $\log(U_H) = -0.4^{+0.4}_{-0.2}$ (see § 3.1 and Fig. 5). This model gives a good match for the UV data of that epoch (2002) and its $\log(U_H)$ is in between those of WA components A [$\log(U_H) = -0.8$] and B [$\log(U_H) = -0.1$]. However, there are two inconsistencies between the models. First, components A and B have a total $\log(N_H) = 20.95 \pm 0.1$ or about 2σ disagreement with that of UV component 1. This discrepancy is mainly due to the limit on the O VII N_{ion} that arises from the bound-free edge of this ion in the X-ray data. In the WA model, about 95% of the O VII N_{ion} arises from components A and B. Second, the reported velocity centroids for WA components A and B (-588 ± 34 km s⁻¹ and -547 ± 31 km s⁻¹, respectively) are in disagreement with the velocity centroids of UV component 1 (-1160 km s⁻¹) and its 300 km s⁻¹ width.

UV component 3 has a velocity centroid at -640 km s⁻¹ and a width of ~ 200 km s⁻¹, and therefore is a better velocity match with WA components A and B. The large uncertainties in the inferred N_H and U_H for UV component 3 (see Fig. 6 and Table 1), make these values consistent with the N_H and U_H deduced

for WA components A and B. However, the uncertainties also allow UV component 3 to have a negligible N_H compared to WA components A and B.

We note that with the current analyses, the better the agreement between UV component 3 and WA components A and B, the worse is the disagreement between UV component 1 and WA components A and B. This is because UV component 1 already predicts higher values of N_H and $O_{VII} N_{ion}$ than are measured in WA components A and B, and the kinematics of the deduced $O_{VII} N_{ion}$ disagree considerably. In points 5 and 6 below we identify two possible ways to alleviate and even eliminate these apparent discrepancies.

5. Existence of considerable $O_{VII} N_{ion}$ at the velocity of UV component 1. The 2002 X-ray spectra presented by Steenbrugge et al. (2005) consist of two different data sets that were acquired in the same week: 170 ks observations taken with the High Energy Transmission Grating Spectrometer (HETGS) and 340 ks observations with the Low Energy Transmission Grating Spectrometer (LETGS). Figure 2 in Steenbrugge et al. (2005) shows some of the low ionization WA troughs in velocity presentation, where the dotted lines show the position of the UV components (with somewhat different velocity values than we use here due to the use of a slightly different systemic redshift for the object). The LETGS data of the O_{VII} and O_V troughs are consistent with one main kinematic component matching the velocity of UV component 3. However, the more noisy but higher resolution HETGS data for the same transitions, show two sub troughs one corresponding to UV component 1 and one to UV component 3. Therefore, it is possible that much of the $O_{VII} N_{ion}$ is associated with UV component 1.

6. Abundances considerations: As mentioned in § 3, for the UV analysis, we use pure proto-Solar abundances (Lodders et al. 2009), which well-match the measured N_{ion} from the UV data. But these models produce considerably more $O_{VII} N_{ion}$ in the 2002 epoch, than the measured $O_{VII} N_{ion}$ in the warm absorber data. However, the N_H (and therefore also the $O_{VII} N_{ion}$) of UV component 1 is critically dependent on the assumed phosphorus abundance. Ionization models with all elements having proto-Solar abundances except phosphorus, for which we assume twice proto-Solar abundance, preserve the fit to the UV data (at 1/3 the N_H value) and at the same time match the $O_{VII} N_{ion}$ measured in the X-ray warm absorber at the 2002 epoch. Larger over-abundances of phosphorus further reduce the N_H value and therefore the predicted $O_{VII} N_{ion}$ for the 2002 epoch.

But are such assumed abundances physically reasonable? AGN outflows are known to have abundances higher by factors of two (Arav et al. 2007) and even ten (Gabel et al. 2006) compared with the proto-Solar values. In particular, phosphorus abundance in AGN outflows, relative to other metals, can be a factor of several higher than in proto-Solar abundances (see §4.1 in Arav et al. 2001). Furthermore, the theoretical expectations for the value of chemical abundances in an AGN environment as a function of metallicity are highly varied. The leading models can differ about relative abundances values by factors of three or more (e.g., comparing the values of Hamann & Ferland 1993; Ballero et al. 2008).

We conclude that if roughly half of the observed $O_{VII} N_{ion}$ is associated with UV component 1 (as discussed in point 5), and if the relative abundance of phosphorus to oxygen is twice solar or larger, than the N_H , U_H and velocity distribution of the WA and UV outflowing gas can be consistent.

6. Discussion

6.1. Comparison With Previous Work

How do these results compare with the previous extensive work on the enduring outflow in NGC 5548? For the first time a simple model of a constant N_H absorber yields a physical picture that is consistent with the substantial trough variation seen in all epochs of high resolution UV spectral observations. The trough changes are explained solely by the observed differences in the incident ionizing flux. In addition, we determine robust distances for (or limits on) all 6 kinematic components. Our results differ considerably from those previously found for this outflow (e.g., Crenshaw et al. 2009). This is due to the powerful diagnostics that were revealed during the 2013 campaign, recognizing that many of the observed troughs are highly saturated (e.g., the existence of similar depth C IV and P V troughs in component 1; see discussion in Borguet et al. 2012a) and the fact that the previous work did not account for the emergence of Si III troughs associated with components 1 and 3 in the 2004 data.

6.2. Implications for BAL Variability Studies

Our multiwavelength campaign has significant consequences for studies of absorption trough variability in quasar outflows, and in particular for the intensive studies of trough variability in Broad Absorption Line (BAL) quasars (e.g., Barlow et al. 1992; Capellupo et al. 2012; Filiz Ak et al. 2013, and references therein). As discussed in § 3.3, the two main proposed mechanisms for trough variability are (1) reaction to changes in ionizing flux of a constant absorber (which is the model we successfully use to explain the NGC 5548 outflow trough changes); and (2) absorber motion across the line of sight (e.g., Gabel et al. 2003), which as we demonstrated, cannot explain the variability of the NGC 5548 outflow (see § 3.3).

In some BAL cases the rest-frame UV flux around 1350 Å does not change appreciably between the studied epochs while significant trough variability is observed. This behavior is taken as an argument against mechanism (1) (e.g., Barlow et al. 1992; Filiz Ak et al. 2013) as the ionizing flux (below 912Å) is assumed to correlate with the longer wavelength UV flux. However, our simultaneous UV/X-ray observations show a clear case where the ionizing photon flux drops by a factor of 25 between the 2002 and 2013 epochs, while the 1350 Å UV flux actually increases by 50%.

The spectroscopic data set of NGC 5548 gives high S/N and high-resolution spectra of many UV absorption troughs, and simultaneously yields the crucial soft X-ray flux that is responsible for the ionization of the outflow. Such data can constrain trough variability models far better than the standard variability data sets where one or two rest-frame UV BAL are observed at two (and less frequently in more) epochs (e.g., Capellupo et al. 2012; Filiz Ak et al. 2013).

6.3. Implications for the X-ray Obscurer

What do our results about the enduring outflow tell us about the X-ray obscurer and the broad UV absorption discovered by Kaastra et al. (2014)? The derived transmission for the X-ray obscurer is consistent with the SED required for the 2013 spectrum, thus showing that the obscurer is closer to the super massive black holes than 3.5 pc., and that its shadow influences the conditions in the more distant narrow UV absorbers.

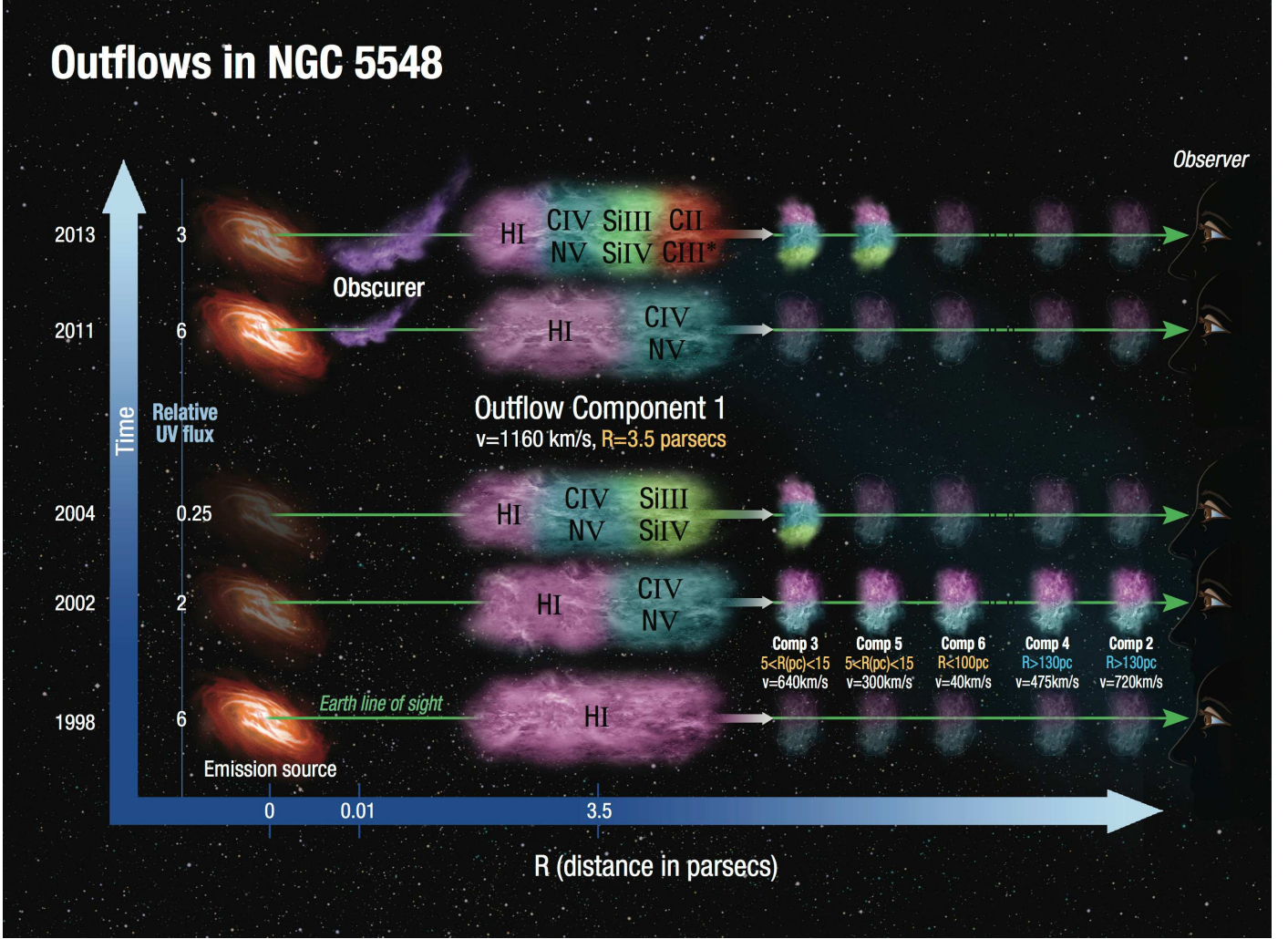


Fig. 7. An illustration of the physical, spatial and temporal conditions of the outflows seen in NGC 5548. Along the time axis we show the behavior of the emission source at the 5 UV epochs and give its UV flux values (measured at 1350 \AA rest-frame and given in units of $10^{-14} \text{ ergs s}^{-1} \text{ cm}^{-2} \text{ \AA}^{-1}$). The obscurer is situated at roughly 0.01 pc from the emission source and is only seen in 2011 and 2013 (it is much stronger in 2013). Outflow component 1 shows the most dramatic changes in its absorption troughs. Different observed ionic species are represented as colored zones within the absorbers. The trough changes are fully explained by our physical model shown in Figure 5. Using component 1 C III^* troughs, which are only seen in the 2013 epoch, we determine its number density (see Figure 4) to be $\log(n_e) = 4.8 \pm 0.1 \text{ cm}^{-3}$, and therefore its distance, $R=3.5$ parsec. The distances for the other components are discussed in § 4. Dimmer clouds represent epochs where components 2-6 did not show new absorption species compared with the 2002 epoch.

7. Summary

In 2013 we executed the most comprehensive multiwavelength spectroscopic campaign on any AGN to date, directed at NGC 5548. This paper presents the analysis' results from our HST/COS data of the often observed UV outflow, which is detected in 6 distinct kinematic components. Our campaign revealed an unusually strong X-ray obscuration. The resulting dramatic decrease in incident ionizing flux on the outflow allowed us to construct a comprehensive physical, spatial and temporal picture for the well-studied AGN wind in this object. Our main findings are listed below (see Fig. 7 for a graphic illustration of our results).

1. Our best constraints are obtained for component 1 (the highest velocity component): It is situated at 3.5 ± 1 pc from the central source, has a total hydrogen column density

of $\log(N_H) = 21.5^{+0.4}_{-0.2} \text{ cm}^{-2}$, an ionization parameter of $\log(U_H) = -1.5^{+0.4}_{-0.2}$, and an electron number density of $\log(n_e) = 4.8 \pm 0.1 \text{ cm}^{-3}$. This component probably carries the largest N_H associated with the UV outflow. See § 3.1 and § 3.2 for elaboration.

2. For component 1 a simple model based on a fixed total column-density absorber, reacting to changes in ionizing illumination, matches the very different ionization states seen at five spectroscopic epochs spanning 16 years. See § 3.3 for elaboration.
3. The wealth of observational constraints makes our changes-of-ionization model a leading contender for interpreting trough variability data of quasar outflows, in particular Broad Absorption Line (BAL) variability. See § 6.2 for elaboration.
4. Components 3 and 5 are situated between 5-15 pc from the central source, component 6 is closer than 100 pc and com-

ponents 2 and 4 are further out than 130 pc. See § 4 for elaboration.

5. A detailed comparison of the physical characteristics inferred from the outflows' UV diagnostics with those of the X-ray Warm Absorber is deferred to a future paper. Here we outline some of the main points in such a comparison, and discuss some of the similarities and challenges of such a combined analysis. See § 5 for elaboration.

Acknowledgements. This work was supported by NASA through grants for HST program number 13184 from the Space Telescope Science Institute, which is operated by the Association of Universities for Research in Astronomy, Incorporated, under NASA contract NAS5-26555. SRON is supported financially by NWO, the Netherlands Organization for Scientific Research. M.M. acknowledges the support of a Studentship Enhancement Programme awarded by the UK Science & Technology Facilities Council (STFC). P.-O.P. and F.U. thanks financial support from the CNES and from the CNRS/PICS. F.U. acknowledges PhD funding from the VINCI program of the French-Italian University. K.C.S. wants to acknowledge financial support from the Fondo Fortalecimiento de la Productividad Científica VRIDT 2013. E.B. is supported by grants from Israel's MoST, ISF (1163/10), and I-CORE program (1937/12). J.M. acknowledges funding from CNRS/PNHE and CNRS/PICS in France. G.M. and F.U. acknowledge financial support from the Italian Space Agency under grant ASI/INAF I/037/12/0-011/13. B.M.P. acknowledges support from the US NSF through grant AST-1008882. M.C, S.B, G.M and A. D. R., acknowledge INAF/PICS support. G.P. acknowledges support via an EU Marie Curie Intra-European fellowship under contract no. FP-PEOPLE-2012-IEF-331095. M. W. acknowledges the support of a PhD studentship awarded by the UK Science & Technology Facilities Council (STFC).

The data used in this research are stored in the public archives of the satellites that are involved. We thank the International Space Science Institute (ISSI) in Bern for support. This work is based on observations obtained with XMM-Newton, an ESA science mission with instruments and contributions directly funded by ESA Member States and the USA (NASA). It is also based on observations with INTEGRAL, an ESA project with instrument and science data center funded by ESA member states (especially the PI countries: Denmark, France, Germany, Italy, Switzerland, Spain), Czech Republic, and Poland and with the participation of Russia and the USA. This work made use of data supplied by the UK Swift Science Data Centre at the University of Leicester. This research made use of the Chandra Transmission Grating Catalog and archive (<http://tgcat.mit.edu>). This research has made use of data obtained with the NuSTAR mission, a project led by the California Institute of Technology (Caltech), managed by the Jet Propulsion Laboratory (JPL) and funded by NASA, and has utilized the NuSTAR Data Analysis Software (NUSTARDAS) jointly developed by the ASI Science Data Center (ASDC, Italy) and Caltech (USA). Figure 7 was created by Ann Feild from STScI.

References

- Arav, N., Becker, R. H., Laurent-Muehleisen, S. A., et al. 1999, *ApJ*, 524, 566
 Arav, N., Borguet, B., Chamberlain, C., Edmonds, D., & Danforth, C. 2013, *MNRAS*, 436, 3286
 Arav, N., de Kool, M., Korista, K. T., et al. 2001, *ApJ*, 561, 118
 Arav, N., Edmonds, D., Borguet, B., et al. 2012, *A&A*, 544, A33
 Arav, N., Gabel, J. R., Korista, K. T., et al. 2007, *ApJ*, 658, 829
 Arav, N., Kaastra, J., Kriss, G. A., et al. 2005, *ApJ*, 620, 665
 Arav, N., Korista, K. T., & de Kool, M. 2002, *ApJ*, 566, 699
 Arav, N., Moe, M., Costantini, E., et al. 2008, *ApJ*, 681, 954
 Ballero, S. K., Matteucci, F., Ciotti, L., Calura, F., & Padovani, P. 2008, *A&A*, 478, 335
 Barlow, T. A., Junkkarinen, V. T., Burbidge, E. M., et al. 1992, *ApJ*, 397, 81
 Borguet, B. C. J., Arav, N., Edmonds, D., Chamberlain, C., & Benn, C. 2013, *ApJ*, 762, 49
 Borguet, B. C. J., Edmonds, D., Arav, N., Benn, C., & Chamberlain, C. 2012a, *ApJ*, 758, 69
 Borguet, B. C. J., Edmonds, D., Arav, N., Dunn, J., & Kriss, G. A. 2012b, *ApJ*, 751, 107
 Capellupo, D. M., Hamann, F., Shields, J. C., Rodríguez Hidalgo, P., & Barlow, T. A. 2012, *MNRAS*, 422, 3249
 Ciotti, L., Ostriker, J. P., & Proga, D. 2010, *ApJ*, 717, 708
 Costantini, E., Kaastra, J. S., Arav, N., et al. 2007, *A&A*, 461, 121
 Crenshaw, D. M., Kraemer, S. B., Boggess, A., et al. 1999, *ApJ*, 516, 750
 Crenshaw, D. M., Kraemer, S. B., Gabel, J. R., et al. 2003, *ApJ*, 594, 116
 Crenshaw, D. M., Kraemer, S. B., Schmitt, H. R., et al. 2009, *ApJ*, 698, 281
 de Kool, M., Korista, K. T., & Arav, N. 2002, *ApJ*, 580, 54

- de Vaucouleurs, G., de Vaucouleurs, A., Corwin, Jr., H. G., et al. 1991, Third Reference Catalogue of Bright Galaxies. Volume I: Explanations and references. Volume II: Data for galaxies between 0^h and 12^h . Volume III: Data for galaxies between 12^h and 24^h .
 Dere, K. P., Landi, E., Mason, H. E., Monsignori Fossi, B. C., & Young, P. R. 1997, *A&AS*, 125, 149
 Edmonds, D., Borguet, B., Arav, N., et al. 2011, *ApJ*, 739, 7
 Faucher-Giguère, C.-A., Quataert, E., & Murray, N. 2012, *MNRAS*, 420, 1347
 Ferland, G. J., Porter, R. L., van Hoof, P. A. M., et al. 2013, *Rev. Mexicana Astron. Astrofis.*, 49, 137
 Filiz Ak, N., Brandt, W. N., Hall, P. B., et al. 2013, *ApJ*, 777, 168
 Gabel, J. R., Arav, N., & Kim, T. 2006, *ApJ*, 646, 742
 Gabel, J. R., Crenshaw, D. M., Kraemer, S. B., et al. 2003, *ApJ*, 583, 178
 Gabel, J. R., Kraemer, S. B., Crenshaw, D. M., et al. 2005, *ApJ*, 631, 741
 Green, J. C., Froning, C. S., Osterman, S., et al. 2012, *ApJ*, 744, 60
 Hamann, F., Barlow, T. A., Junkkarinen, V., & Burbidge, E. M. 1997, *ApJ*, 478, 80
 Hamann, F. & Ferland, G. 1993, *ApJ*, 418, 11
 Hopkins, P. F. & Elvis, M. 2010, *MNRAS*, 401, 7
 Kaastra, J. S., Detmers, R. G., Mehdipour, M., et al. 2012, *A&A*, 539, A117
 Kaastra et al., J. S. 2014, *Science*
 Korista, K. T., Alloin, D., Barr, P., et al. 1995, *ApJS*, 97, 285
 Landi, E., Young, P. R., Dere, K. P., Del Zanna, G., & Mason, H. E. 2013, *ApJ*, 763, 86
 Lodders, K., Palme, H., & Gail, H.-P. 2009, in "Landolt-Börnstein - Group VI Astronomy and Astrophysics Numerical Data and Functional Relationships in Science and Technology Volume, ed. J. E. Trümper, 44
 Mehdipour et al, M. 2014
 Ostriker, J. P., Choi, E., Ciotti, L., Novak, G. S., & Proga, D. 2010, *ApJ*, 722, 642
 Pancoast, A., Brewer, B. J., Treu, T., et al. 2013, *ArXiv e-prints*
 Schlegel, D. J., Finkbeiner, D. P., & Davis, M. 1998, *ApJ*, 500, 525
 Soker, N. & Meiron, Y. 2011, *MNRAS*, 411, 1803
 Steenbrugge, K. C., Kaastra, J. S., Crenshaw, D. M., et al. 2005, *A&A*, 434, 569

Appendix A: Ionic Column Density Measurements

The column density associated with a given ion as a function of the radial velocity v is defined as:

$$N_{ion}(v) = \frac{3.8 \times 10^{14}}{f_j \lambda_j} \langle \tau_j(v) \rangle \quad (\text{cm}^{-2} \text{ km}^{-1} \text{ s}) \quad (\text{A.1})$$

where f_j , λ_j and $\langle \tau_j(v) \rangle$ are respectively the oscillator strength, the rest wavelength and the average optical depth across the emission source of the line j for which the optical depth solution is derived (see Edmonds et al. 2011). The optical depth solution across a trough is found for a given ion by assuming an absorber model. As shown in Edmonds et al. (2011), the major uncertainty on the derived column densities comes from the choice of absorption model. In this study we investigate the outflow properties using column densities derived from three common absorber models.

Assuming a single, homogeneous emission source of intensity F_0 , the simplest absorber model is the one where a homogeneous absorber parameterized by a single optical depth fully covers the photon source. In that case, known as the apparent optical depth scenario (AOD), the optical depth of a line j as a function of the radial velocity v in the trough is simply derived by the inversion of the Beer-Lambert law : $\tau_j(v) = -\ln(F_j(v)/F_0(v))$, where $F_j(v)$ is the observed intensity of the line.

Early studies of AGN outflows pointed out the inadequacy of such an absorber model, specifically its inability to account for the observed departure of measured optical depth ratio between the components of typical doublet lines from the expected laboratory line strength ratio $R = \lambda_i f_i / \lambda_j f_j$. Two parameter absorber models have been developed to explain such discrepancies. The partial covering model (e.g. Hamann et al. 1997; Arav et al. 1999, 2002, 2005) assumes that only a fraction C of the emission source is covered by absorbing material with constant optical depth τ . In that case, the intensity observed for a line j of a chosen ion can be expressed as

$$F_j(v) = F_0(v)(1 + C(v) * (e^{-\tau_j(v)} - 1)). \quad (\text{A.2})$$

Our third choice are inhomogeneous absorber models. In that scenario, the emission source is totally covered by a smooth distribution of absorbing material across its spatial dimension x . Assuming the typical power law distribution of the optical depth $\tau(x) = \tau_{max} x^a$ (de Kool et al. 2002; Arav et al. 2005, 2008), the observed intensity observed for a line j of a chosen ion is given by

$$F_j(v) = F_0(v) \int_0^1 e^{-\tau_{max,j}(v)x^{a(v)}} dx \quad (\text{A.3})$$

Once the line profiles have been binned on a common velocity scale (we choose a resolution $dv = 20 \text{ km s}^{-1}$, slightly lower than the resolution of COS), a velocity dependent solution can be obtained for the couple of parameters (C, τ_j) or (a, τ_{max}) of both absorber models as long as one observes at least two lines from a given ion, sharing the same lower energy level. Once the velocity dependent solution is computed, the corresponding column density is derived using Equation (A.1) where $\langle \tau_j(v) \rangle = C_{ion}(v)\tau_j(v)$ for the partial covering model and $\langle \tau_j(v) \rangle = \tau_{max,j}(v)/(a_{ion}(v) + 1)$ for the power law distribution. Note that the AOD solution can be computed for any line (singlet or multiplet), without further assumption on the model, but will essentially give a lower limit on the column density when the expected line strength ratio observed is different from the laboratory value.

Table A.1. Observations and flux values for all epochs

Epoch	Observing Dates	Instrument	Grating	Exposure	avg F_{1350}^a	fit F_{1350}^b	fit α^c
2013_v1	2013/06/22	HST:COS	G130M	1.8ks	1.95 ± 0.36		
			G160M	2.1ks			
2013_v2	2013/07/12	HST:COS	G130M	5.0ks	2.22 ± 0.34		
			G160M	2.2ks			
2013_v3	2013/07/24	HST:COS	G130M	2.0ks	3.70 ± 0.44		
			G160M	2.2ks			
2013_v4	2013/07/30	HST:COS	G130M	2.0ks	3.51 ± 0.44		
			G160M	2.2ks			
2013_v5	2013/08/01	HST:COS	G130M	2.0ks	3.28 ± 0.40		
			G160M	2.2ks			
2013_v6	2013/12/20	HST:COS	G130M	2.0ks	3.26 ± 0.40	3.14 ± 0.02	-0.79 ± 0.03
			G160M	2.2ks			
2013_v345	2013/07/24 to 2013/08/01	HST:COS	G130M	6.0ks	3.51 ± 0.24	3.44 ± 0.03	-0.776 ± 0.014
			G160M	6.6ks			
2013_v12345	2013/06/22 to 2013/08/01	HST:COS	G130M	12.8ks	3.11 ± 0.19	3.051 ± 0.015	-0.736 ± 0.026
			G160M	11.0ks			
2011	2011/06/16	HST:COS	G130M	1.9ks	6.17 ± 0.52	6.13 ± 0.05	-0.86 ± 0.07
			G160M	2.4ks			
2004	2004/02/10 to 2004/02/13	HST:STIS	E140M	52.2ks	0.25 ± 0.07	0.203 ± 0.017	-1.86 ± 0.29
2002	2002/01/22 to 2002/01/23	HST:STIS	E140M	15.3ks	1.80 ± 0.18	1.80 ± 0.04	-1.46 ± 0.06
1998	1998/03/11	HST:STIS	E140M	4.75ks	6.41 ± 0.75	6.43 ± 0.12	-1.51 ± 0.13

^aFlux at rest-frame 1350Å in units of 10^{-14} erg s⁻¹ cm⁻² Å⁻¹

^bFlux from a power-law fit of the form $F(\lambda) = F_{1350}(\lambda/1350)^\alpha$

^cSpectral index from the above power-law fit

Table A.2. UV column densities for the outflow components in NGC 5548

Ion	v_1 [-1450, -850] ^a	v_2 [-850, -750]	v_3 [-750, -540]	v_4 [-540, -360]	v_5 [-360, -80]	v_6 [-80, +50]
Epoch 2013						
H I	>14.39 ^b	>13.86	>14.28	>14.40	>14.00	>13.00
C II	>14.52	<12.81	13.67 ^{+0.1} _{-0.1}	<13.24	<13.40	<13.00
C III*	14.03 ^{+0.02} _{-0.02}					
C III ^{j=0}	14.64 ^{+0.02} _{-0.02}					
C III ^{j=2}		14.00 ^{+0.3} _{-0.1}	>14.30	>14.30	>14.10	>13.70
C IV	>14.60					
N v	>14.90	13.90 ^{+0.2} _{-0.2}	>14.90	>14.80	>14.60	>14.10
Al II	>13.05					
Si II	14.30 ^{+0.18} _{-0.3}	<11.80	<12.00	<11.90	<11.40	<12.10
Si III	>13.70	<12.00	13.10 ^{+0.3} _{-0.3}	<12.20	12.20 ^{+0.2} _{-0.2}	<11.50
Si IV	>14.08	12.30 ^{+0.2} _{-0.2}	13.88 ^{+0.2} _{-0.2}	<13.00	13.13 ^{+0.2} _{-0.2}	<12.30
P III	14.04 ^{+0.16} _{-0.06}					
P V	14.15 ^{+0.5} _{-0.15}					
S III	15.00 ^{+0.30} _{-0.2}					
Fe III	14.70 ^{+0.30} _{-0.30}					
Epoch 2011						
H I	>14.34	>13.80	>14.28	>14.33	>13.83	>12.90
C IV	>14.20	>13.70	>14.30	14.40 ^{+0.2} _{-0.2}	>13.83	>13.03
N v	>14.59	>13.95	>14.65	>14.77	>14.43	>13.84
Si III	<12.20	<11.50	<11.98	<11.84	<11.55	<11.59
Si IV	<13.06	<12.54	<12.66	<12.70	<12.53	<12.37
Epoch 2004						
H I	>13.94	>13.82	>14.20	>14.44	>14.15	>12.41
C IV	>14.59	>13.83	>13.95	>14.25	>14.20	>13.16
N v	>14.65	>13.83	>14.20	>14.35	>13.75	>13.20
Si III	>13.61	>12.47	>13.29	>12.41	>12.66	>12.33
Si IV	>14.18	>12.91	>13.65	>12.71	>13.32	>12.76
Epoch 2002						
H I	>14.34	>13.91	>14.29	>14.46	>13.91	>13.20
C IV	>14.08	>13.54	>13.95	14.30 ^{+0.2} _{-0.2}	>13.60	>13.23
N v	>14.54	13.87 ^{+0.2} _{-0.2}	14.50 ^{+0.2} _{-0.2}	>14.76	>14.12	>13.21
Si III	<12.66	<11.80	<11.97	<11.91	<12.14	<11.97
Si IV	<13.31	<12.39	<12.81	<12.74	<13.13	<12.58
Epoch 1998						
H I	>14.06	>13.66	>14.28	>14.36	>13.75	>12.96
C IV	<13.69	>13.25	>13.59	>14.47	<13.09	<13.00
N v	<13.99	>13.89	>14.19	>14.88	>14.13	<13.98
Si III	<12.83	<12.14	<12.46	<12.18	<12.57	<12.41
Si IV	<13.39	<12.83	<12.93	<12.69	<12.89	<12.13

^aIntegration limits in km s⁻¹.^bLower limit log column densities given in units of cm⁻² are shown in blue.
Upper limits are likewise shown in red.

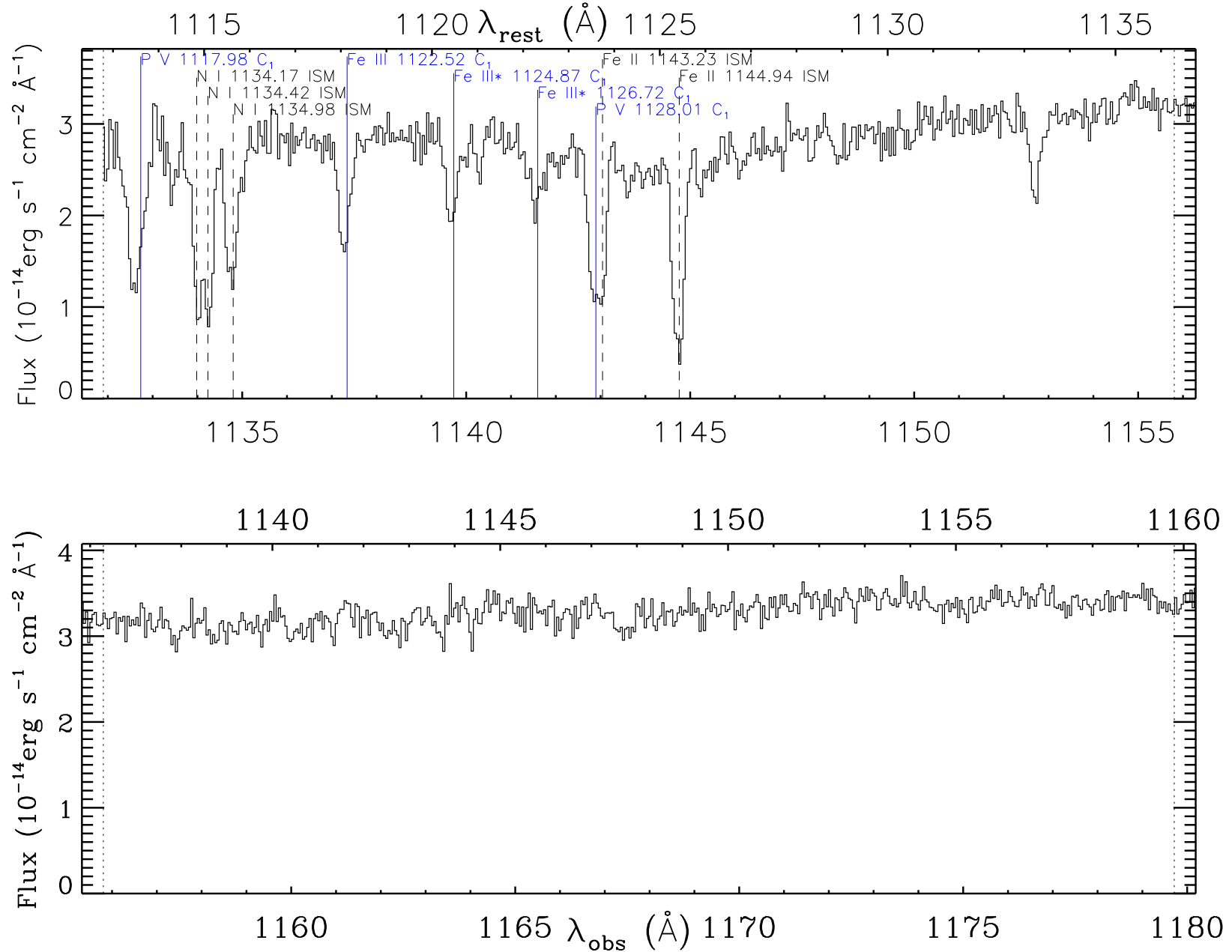


Fig. A.1.a. Plot of the 2013 spectrum of NGC 5548. The vertical axis is the flux in units of $10^{-14} \text{ erg s}^{-1} \text{ cm}^{-2} \text{ \AA}^{-1}$, and the quasar-rest-frame and observer-frame wavelengths are given in Angstroms on the top and bottom of each sub-plot, respectively. Each of the six kinematic components of the outflow shows absorption troughs from several ions. We place a vertical mark at the expected center of each absorption trough (following the velocity template of Si iv and N v) and state the ion, rest-wavelength and component number (C₁–C₆). We also assign a color to each component number that ranges from blue (C₁) to red (C₆). Absorption lines from the ISM are likewise marked in black with dashed lines.

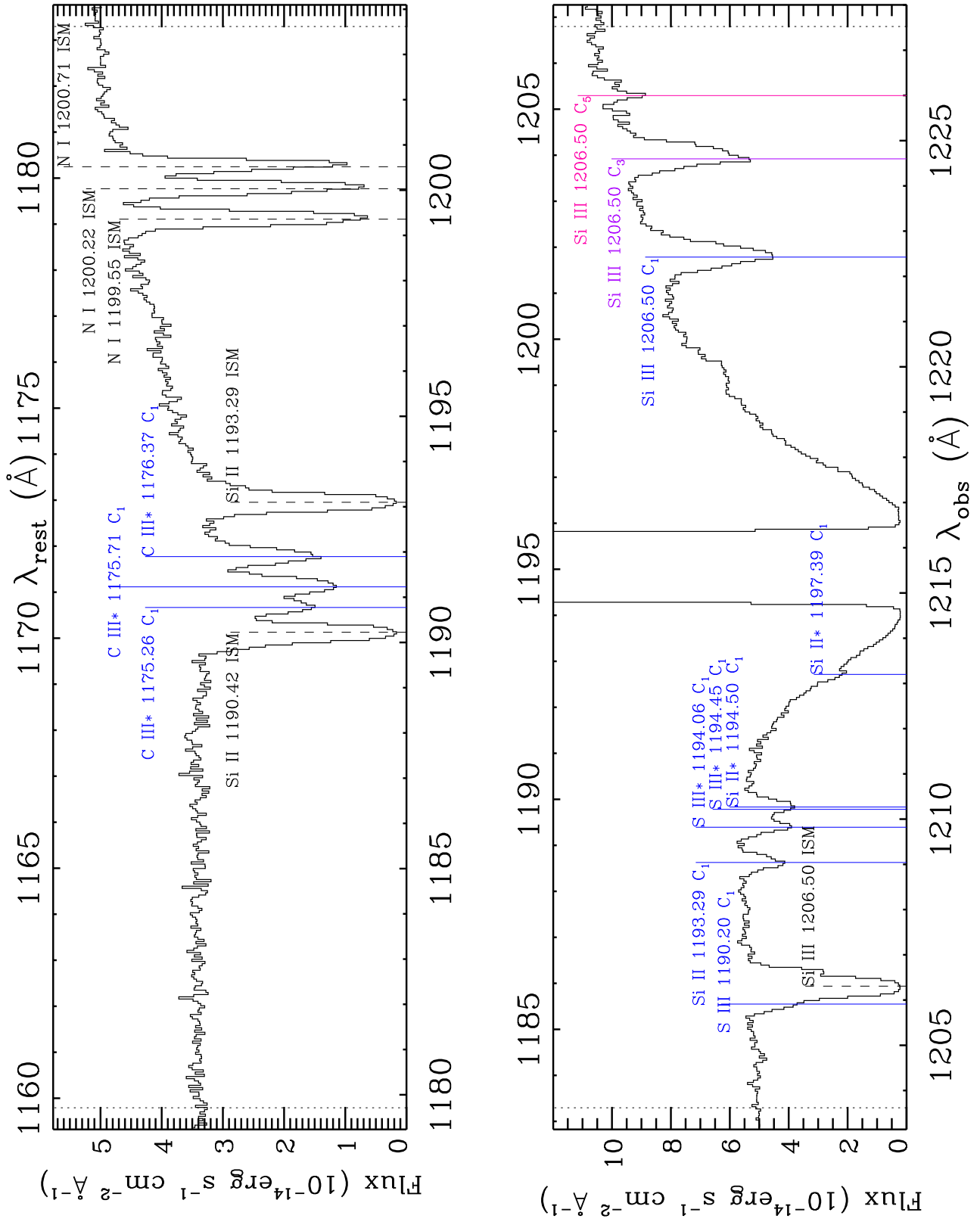


Fig.A.1.b. continued.

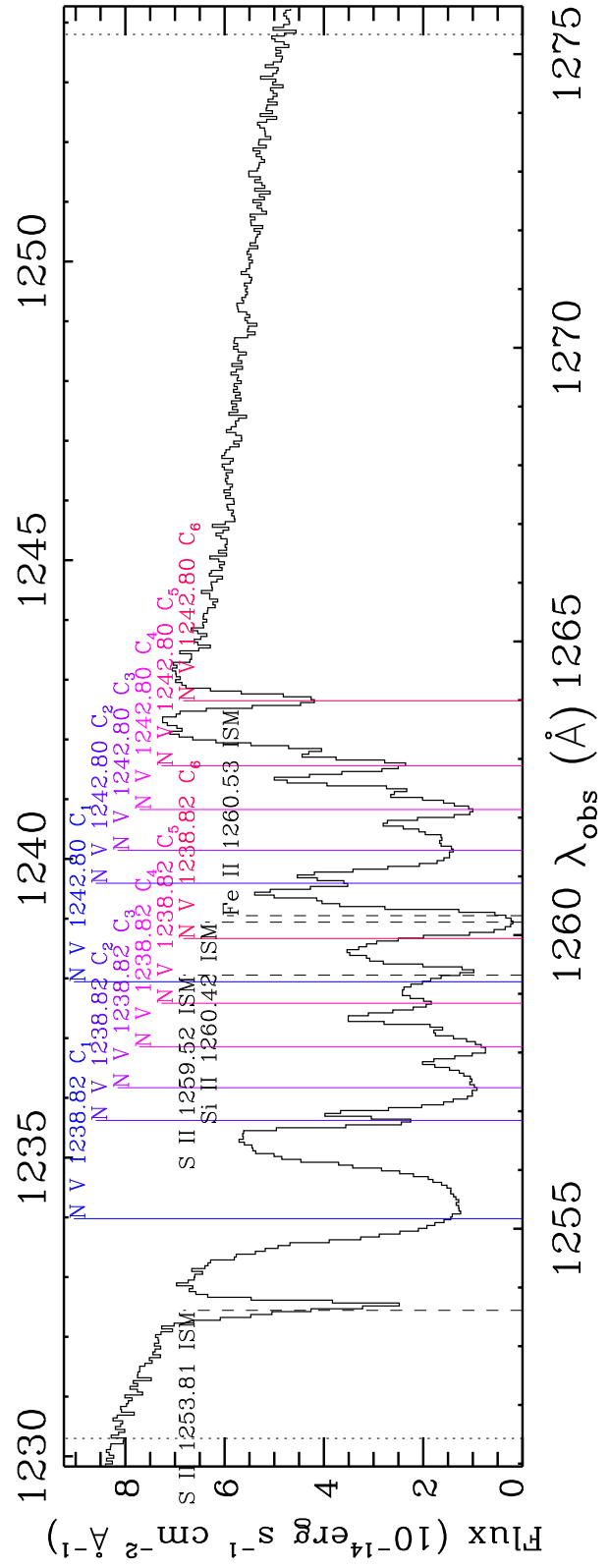
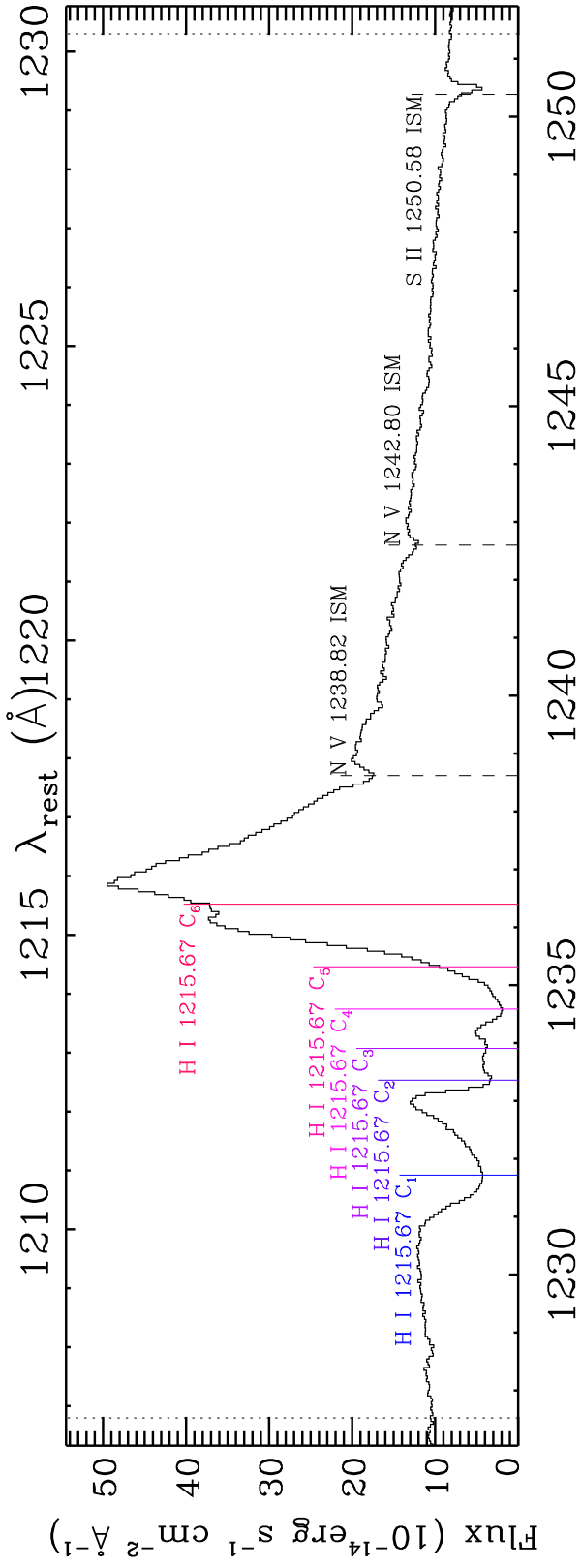


Fig. A.1.c. continued.

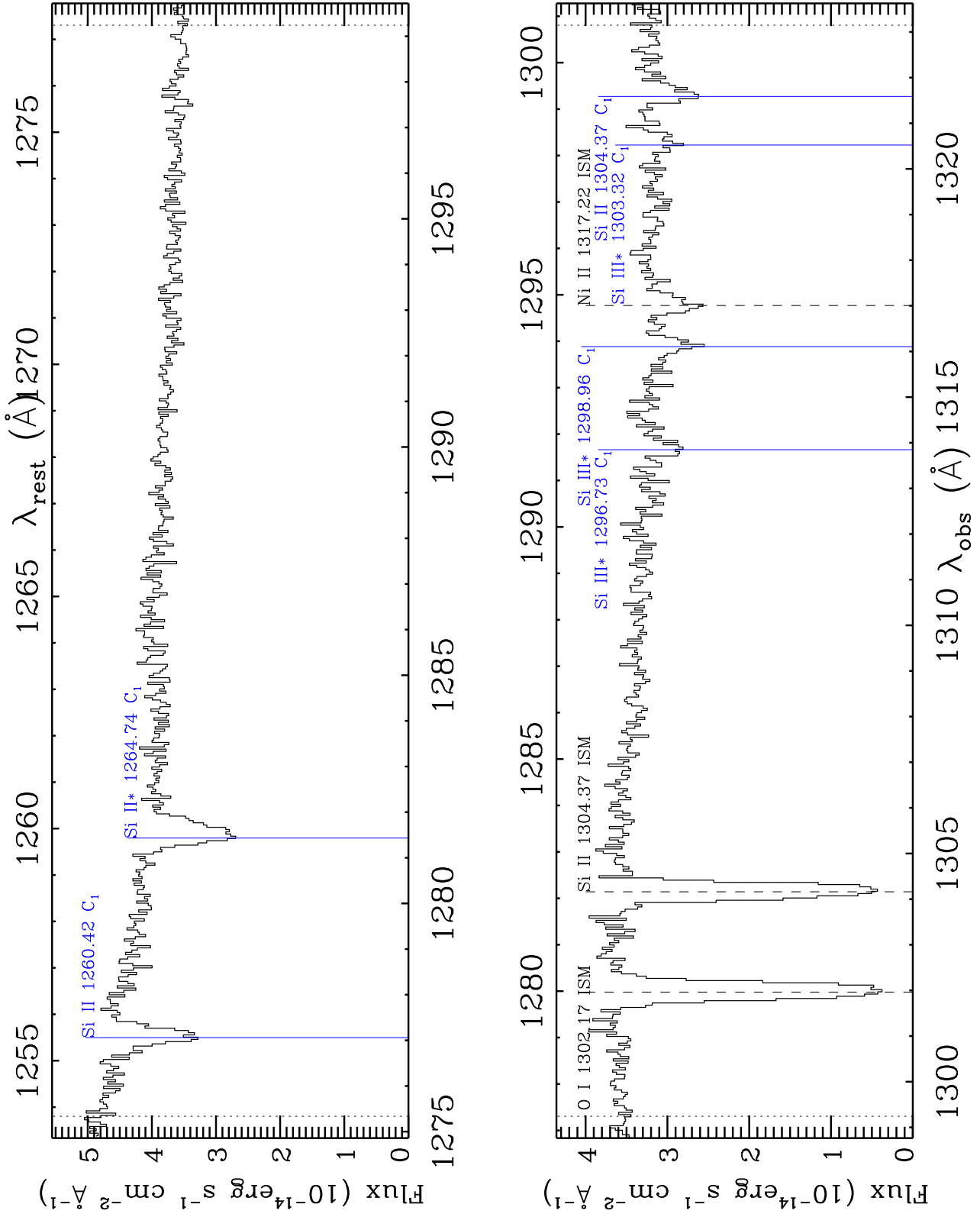


Fig. A.1.d. continued.

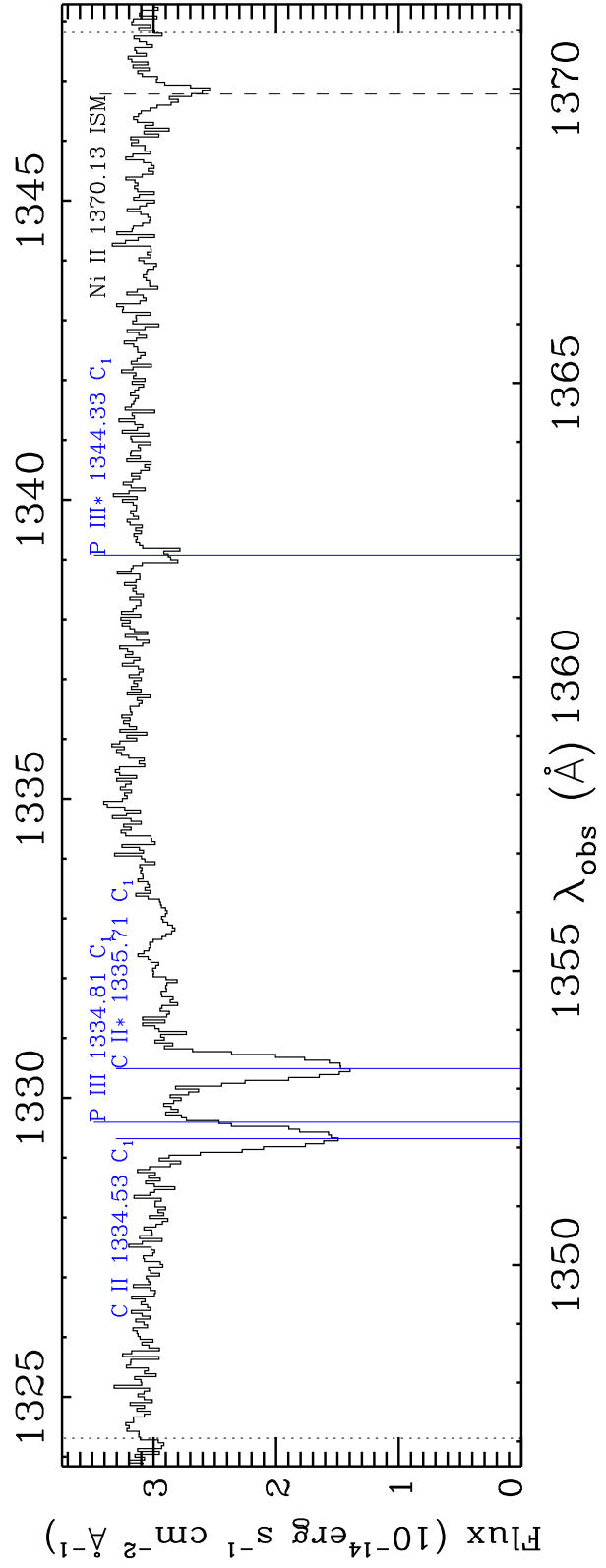
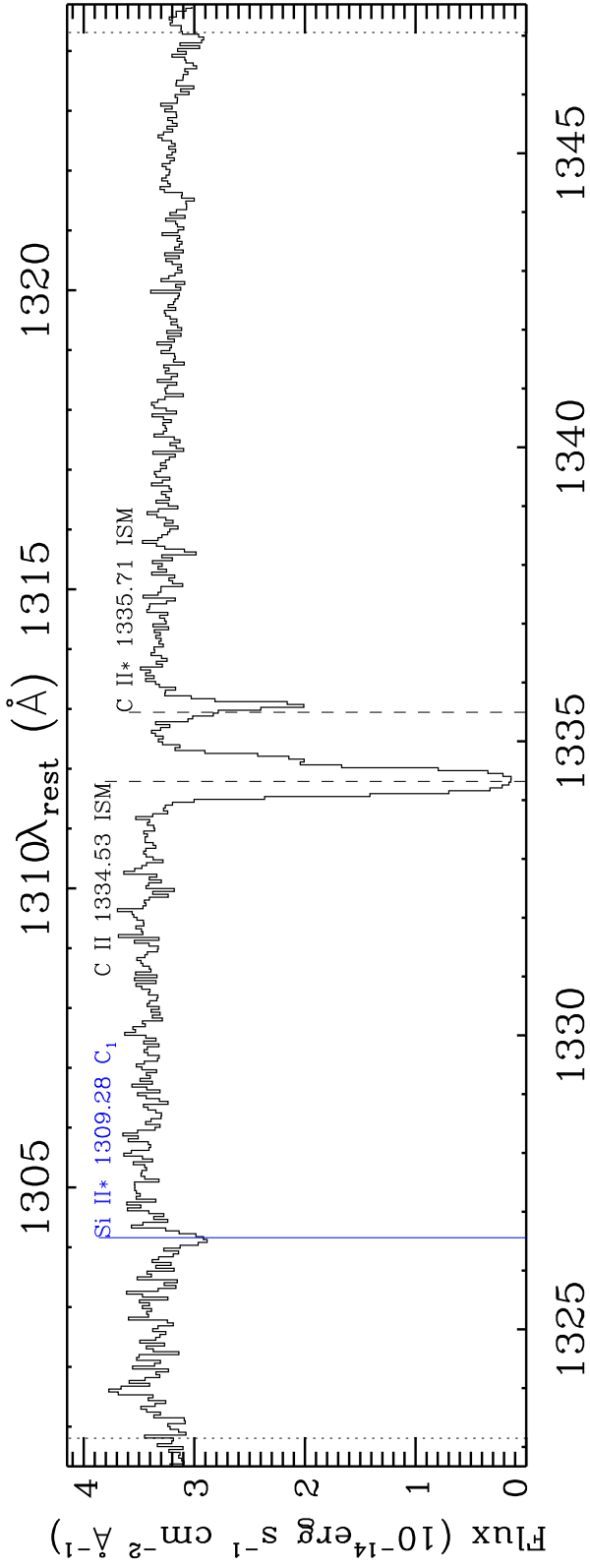


Fig. A.1.e. continued.

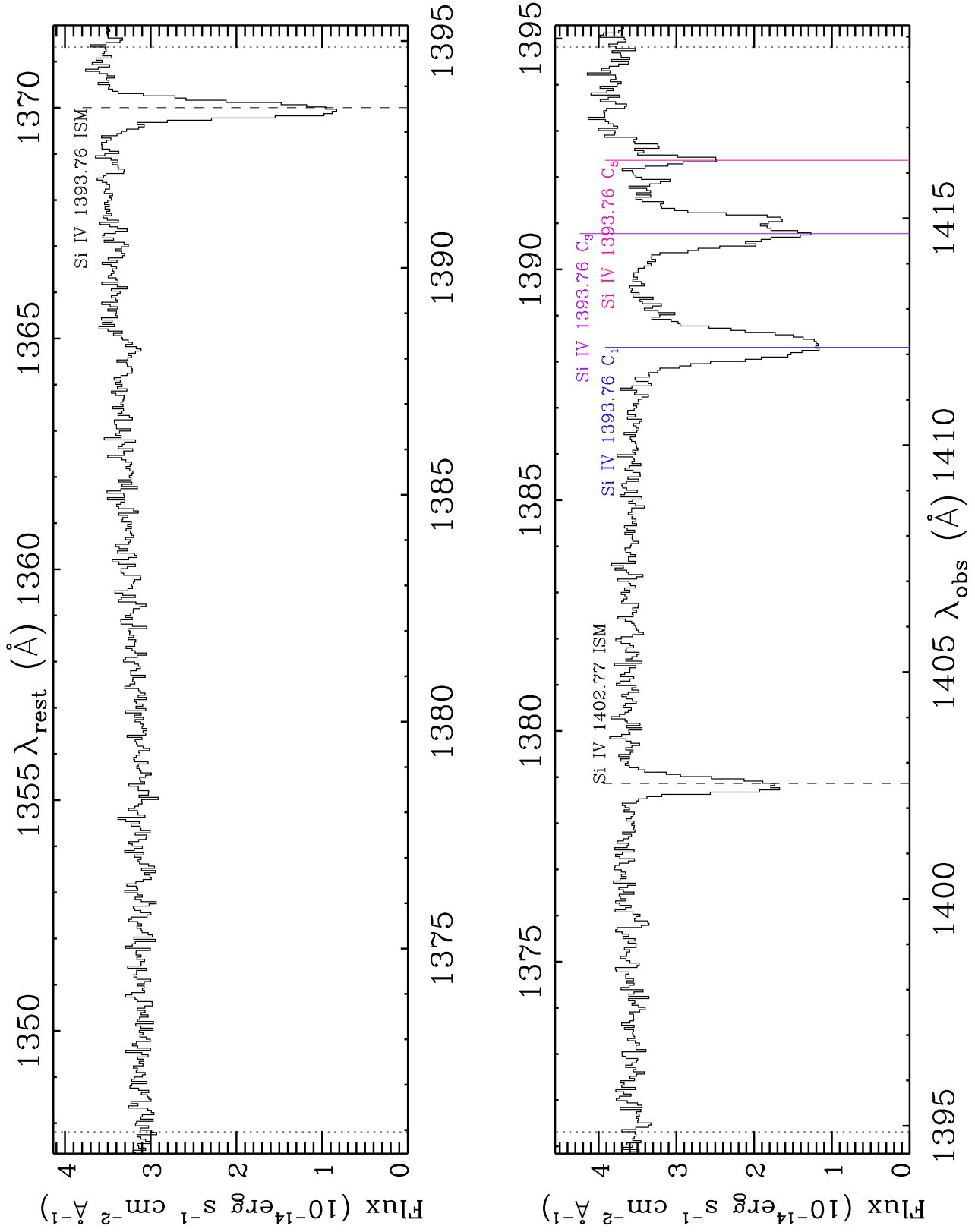


Fig. A.1.f. continued.

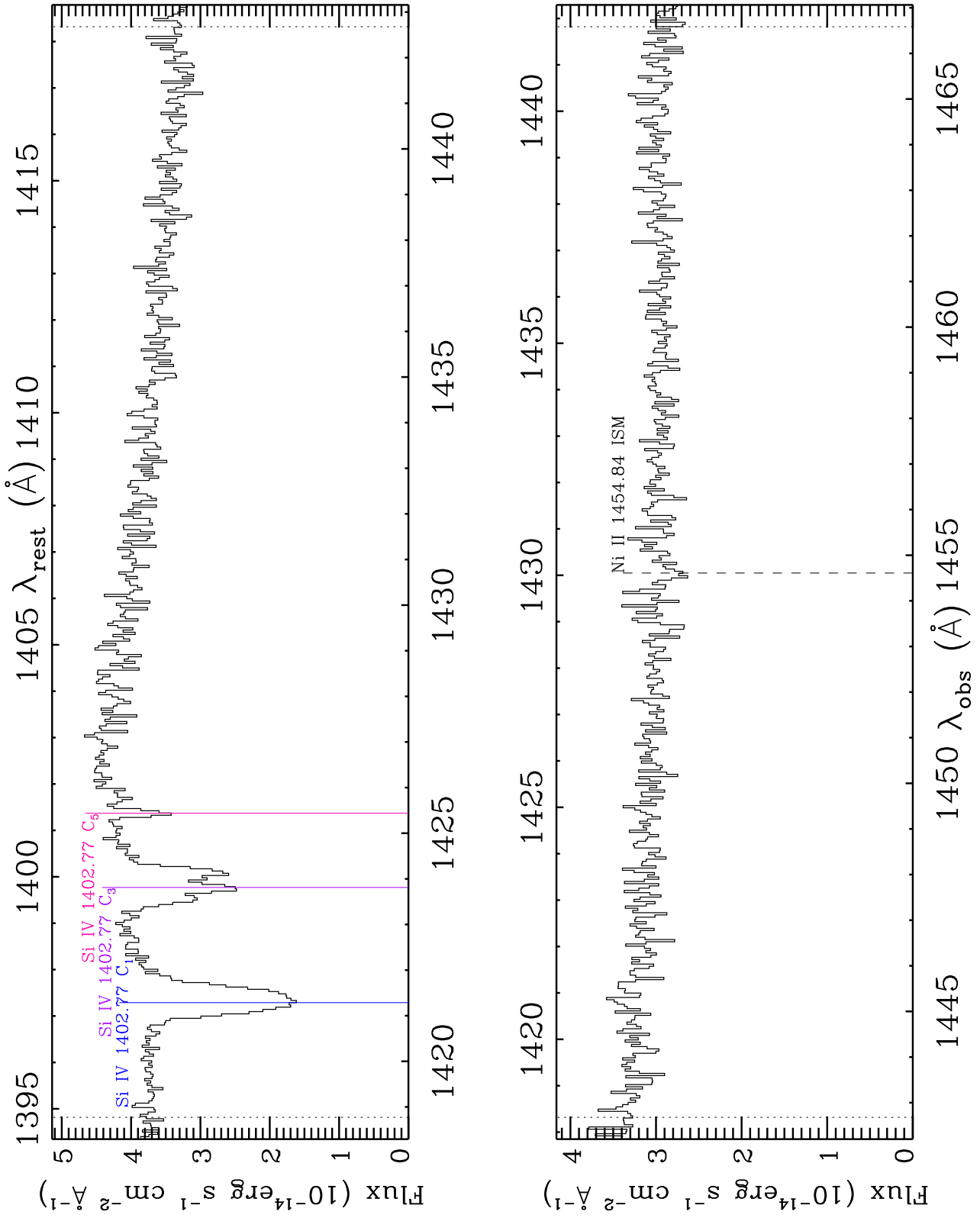


Fig. A.1.g. continued.

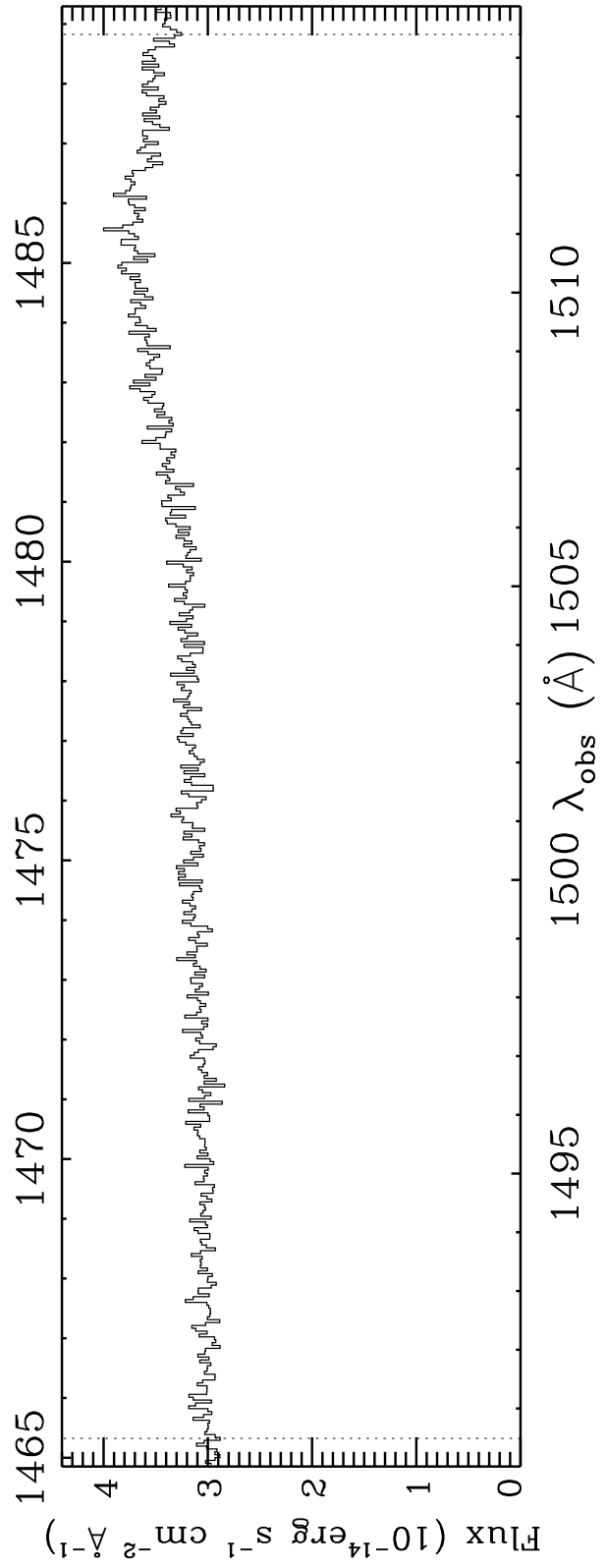
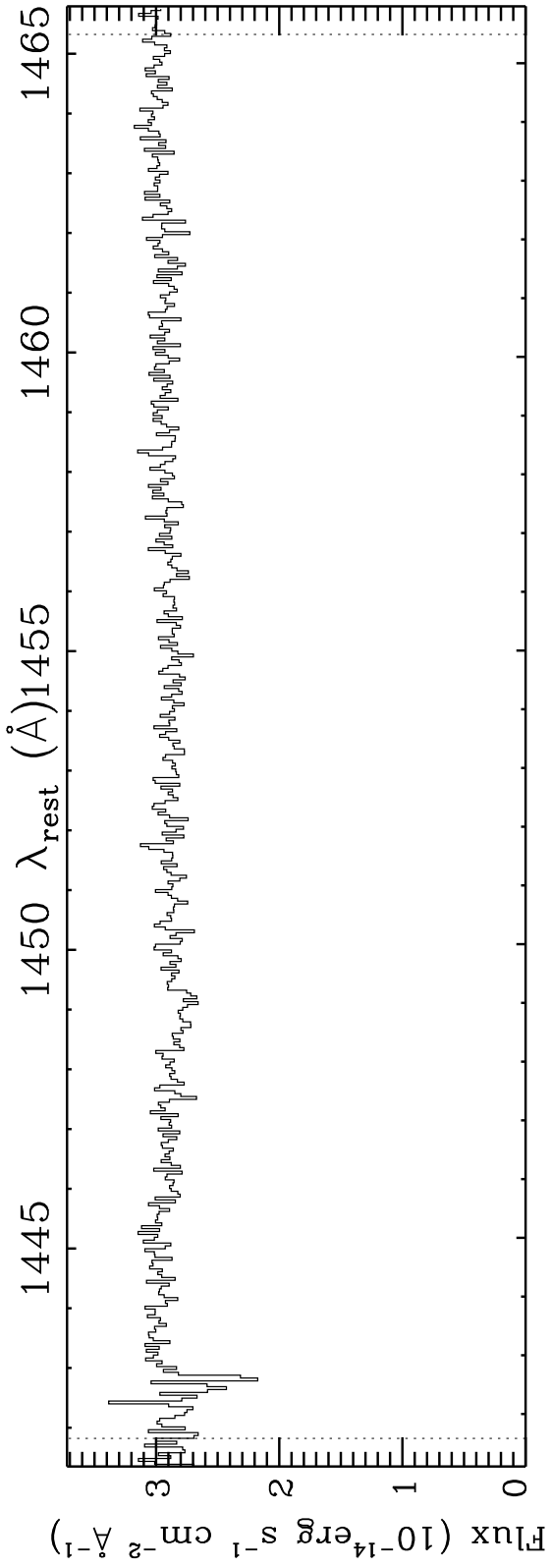


Fig. A.1.h. continued.

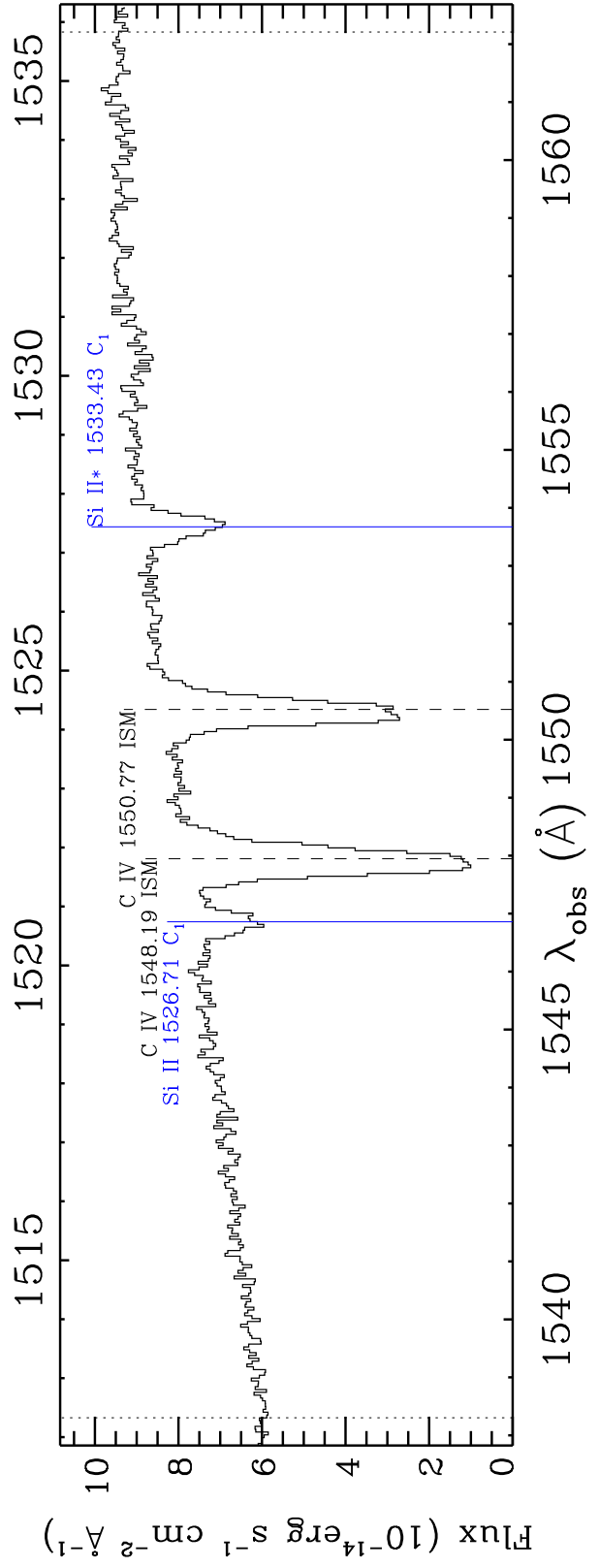
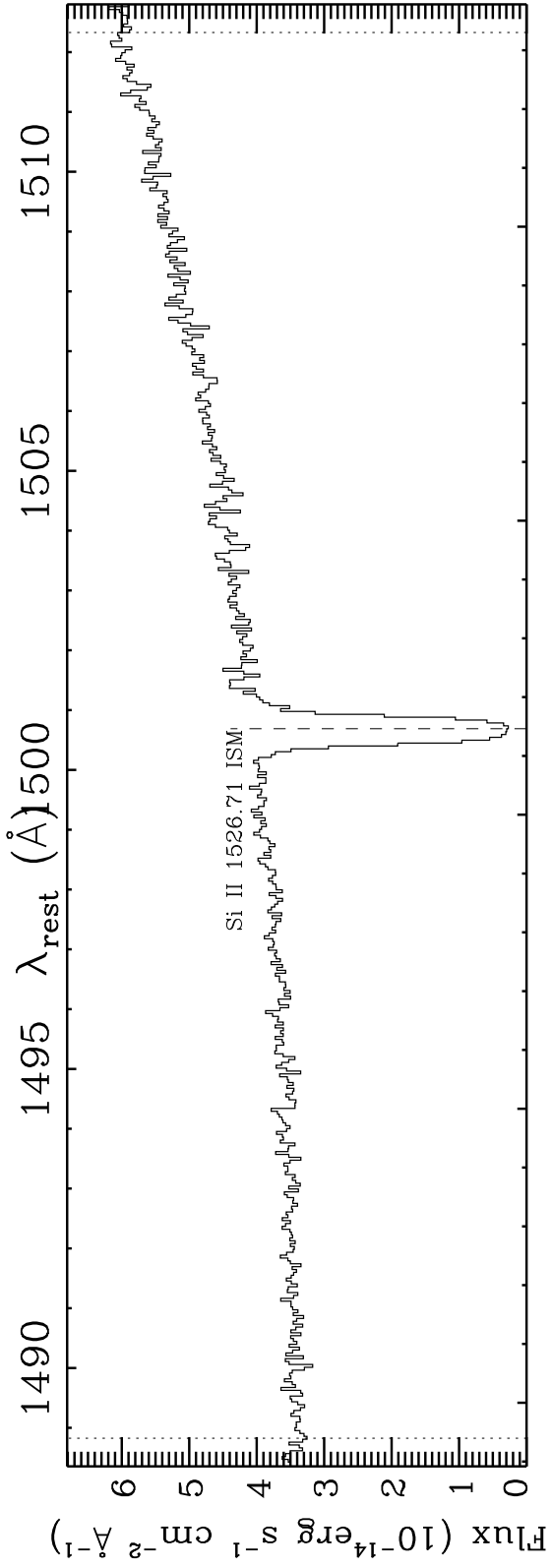


Fig.A.1.i. continued.

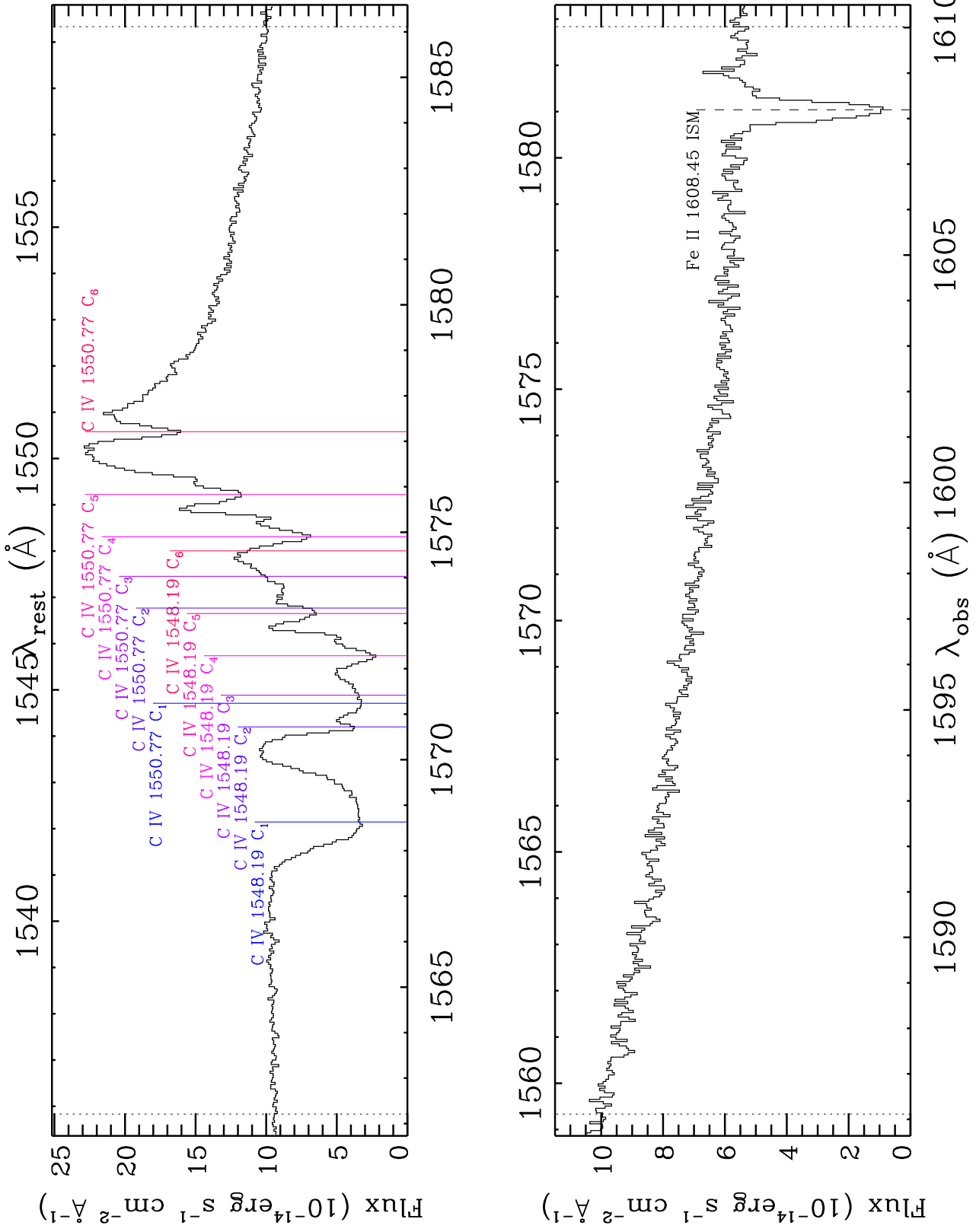


Fig.A.1.j. continued.

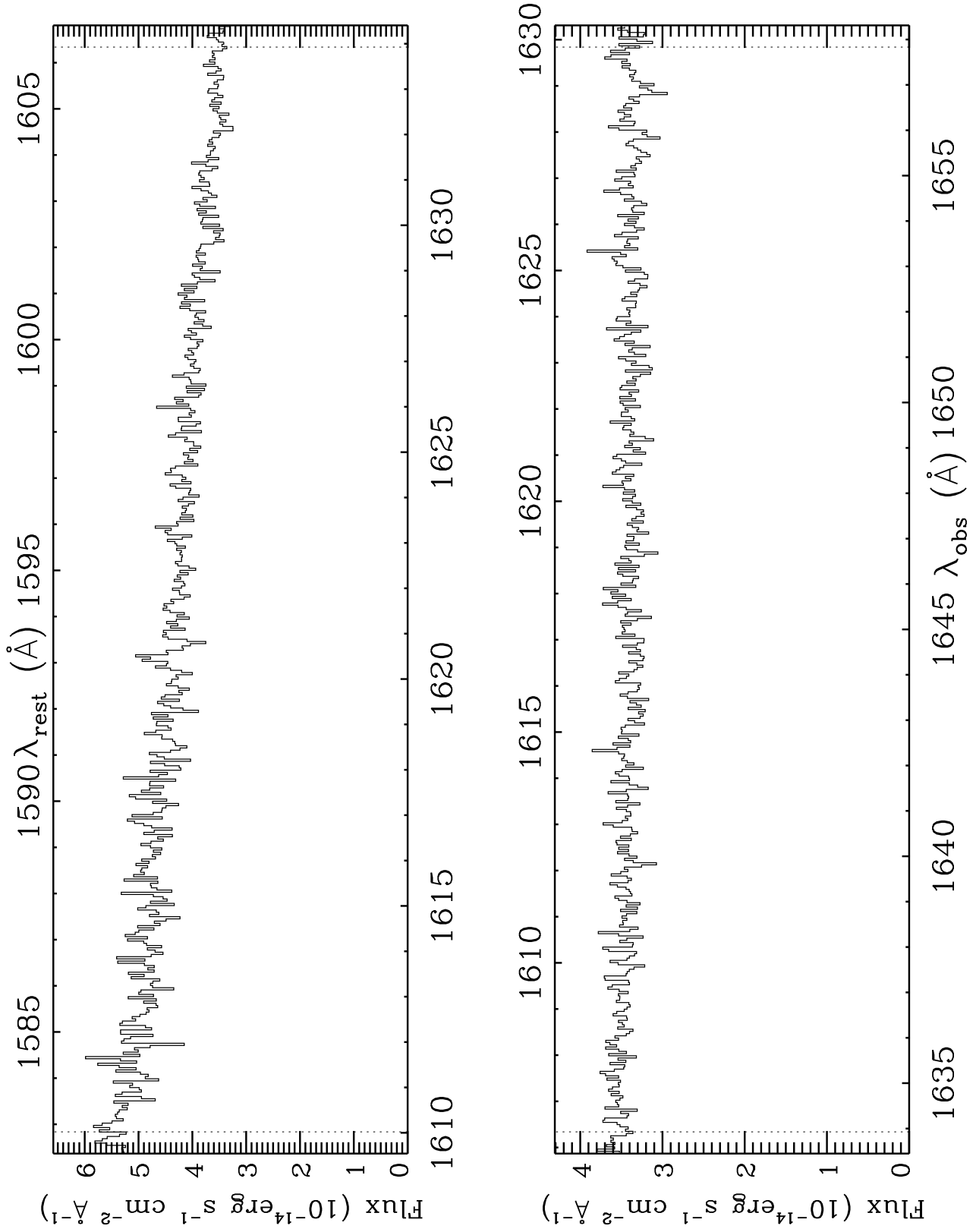


Fig. A.1.k. continued.

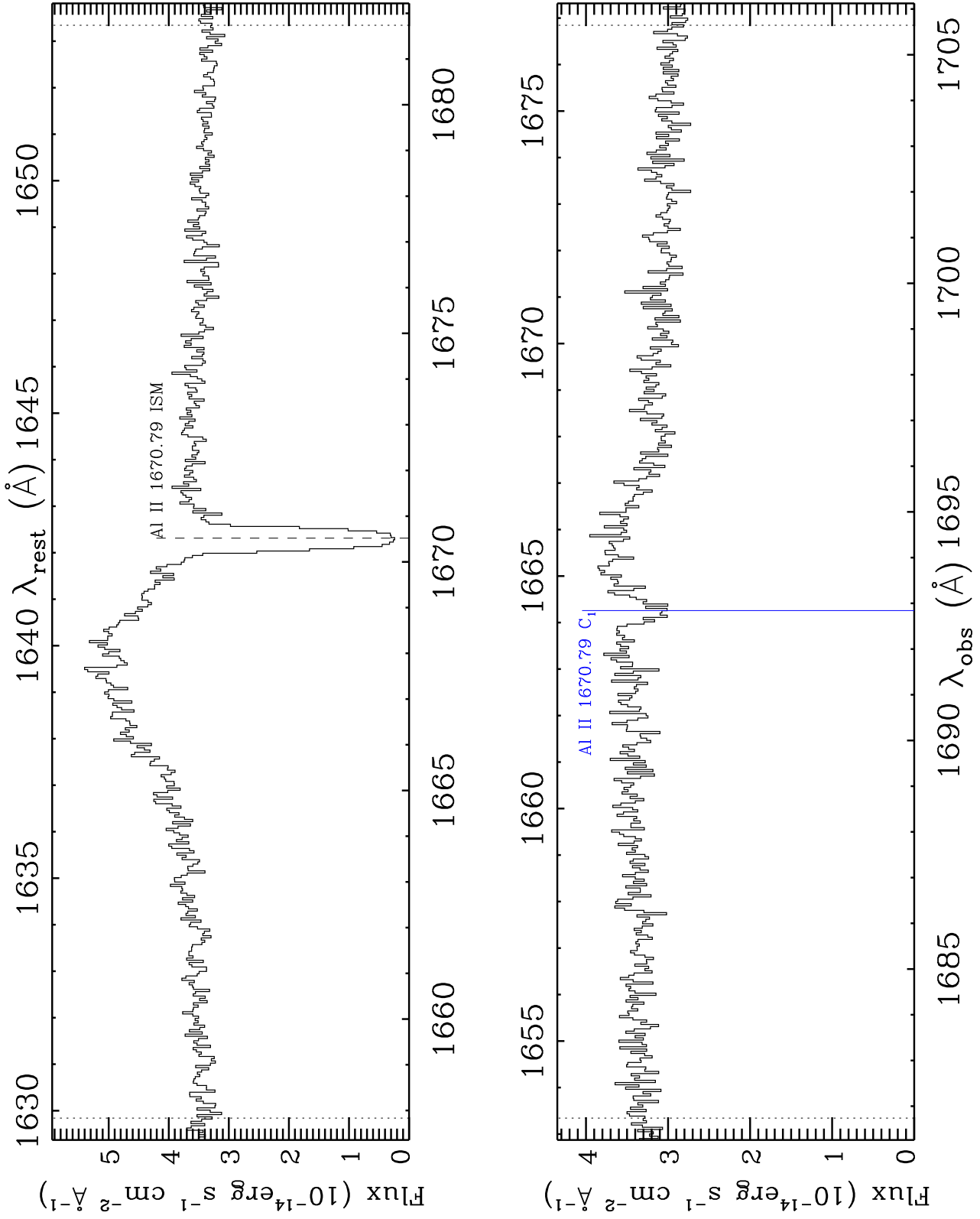


Fig.A.1.I. continued.

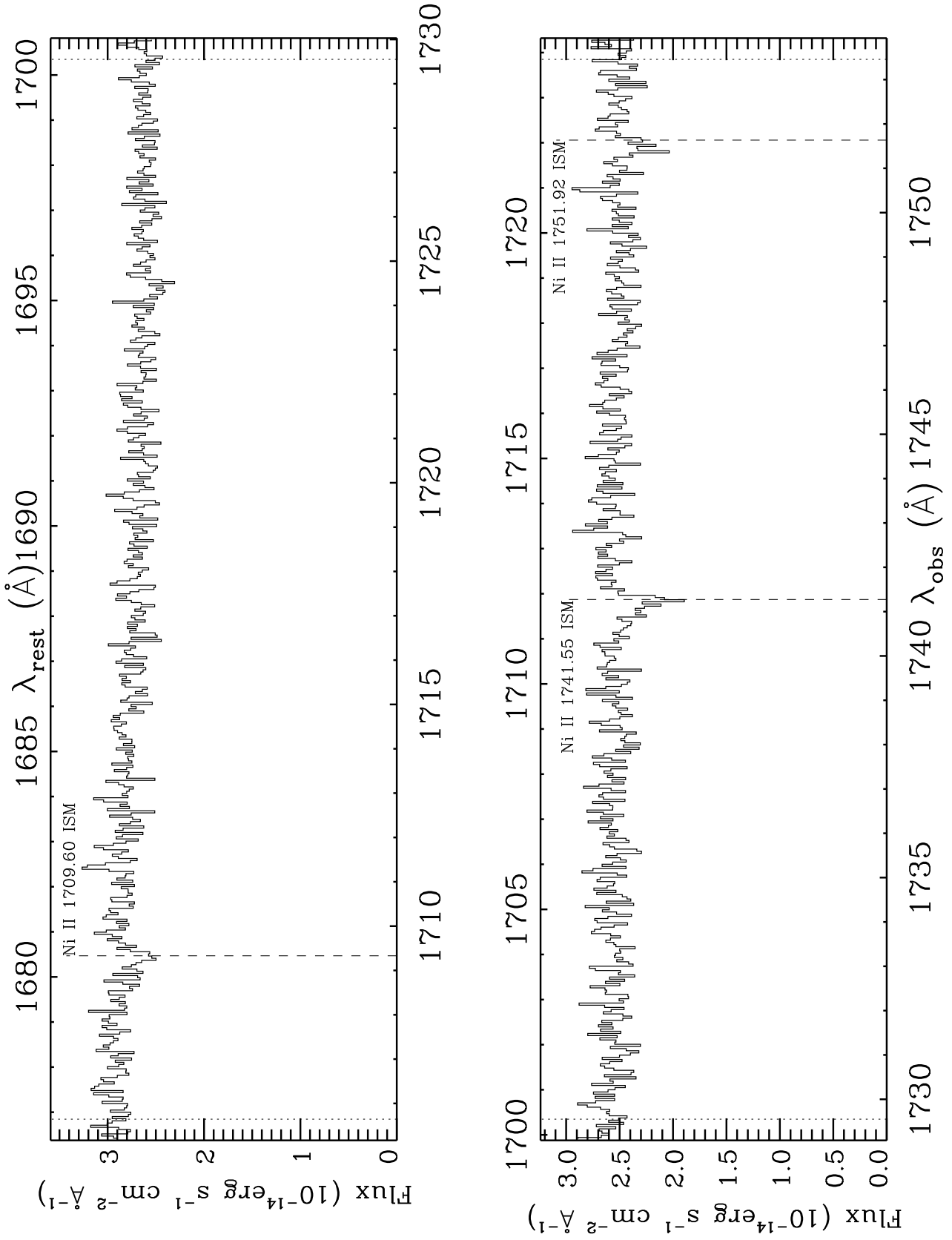


Fig.A.1.m. continued.

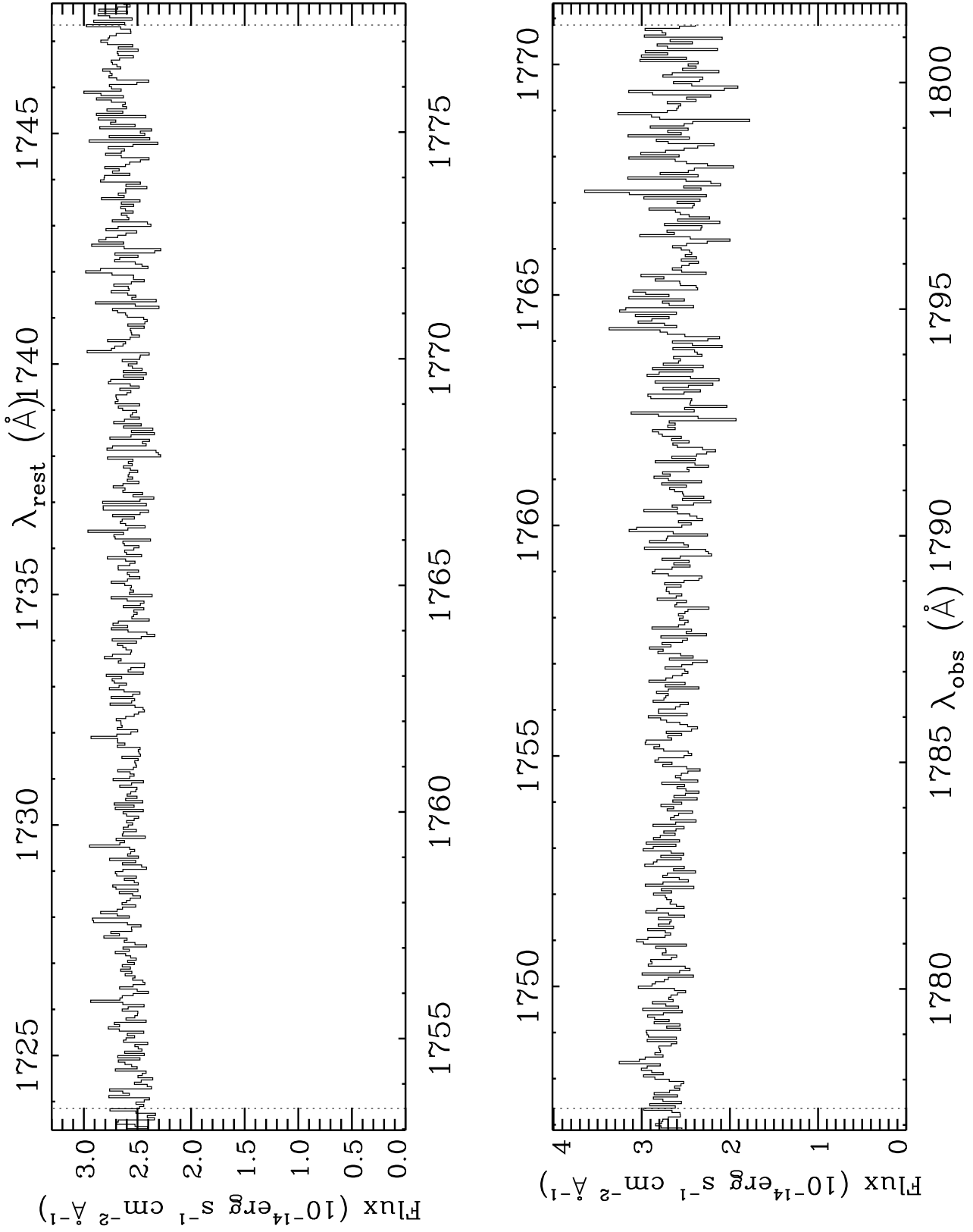


Fig.A.1.n. continued.

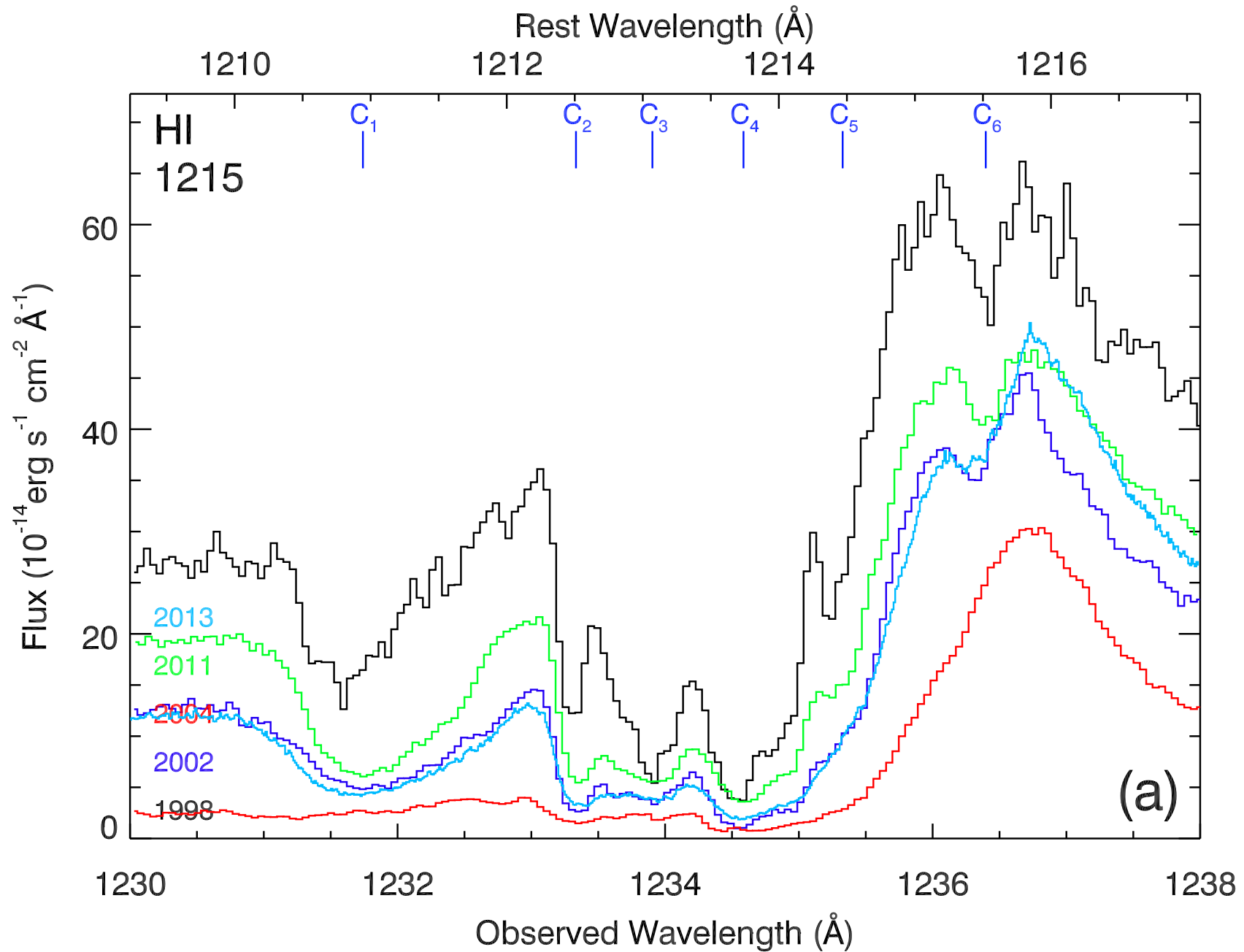


Fig. A.2.a. A plot of the spectrum of NGC 5548 during the five epochs of observation. The 2013 spectrum is obtained by co-adding visits 1 through 5. Spectral regions where absorption troughs from five ions are shown in sub-plots (a) through (e) and the six kinematic components associated with such absorption are labelled C_1 through C_6 .

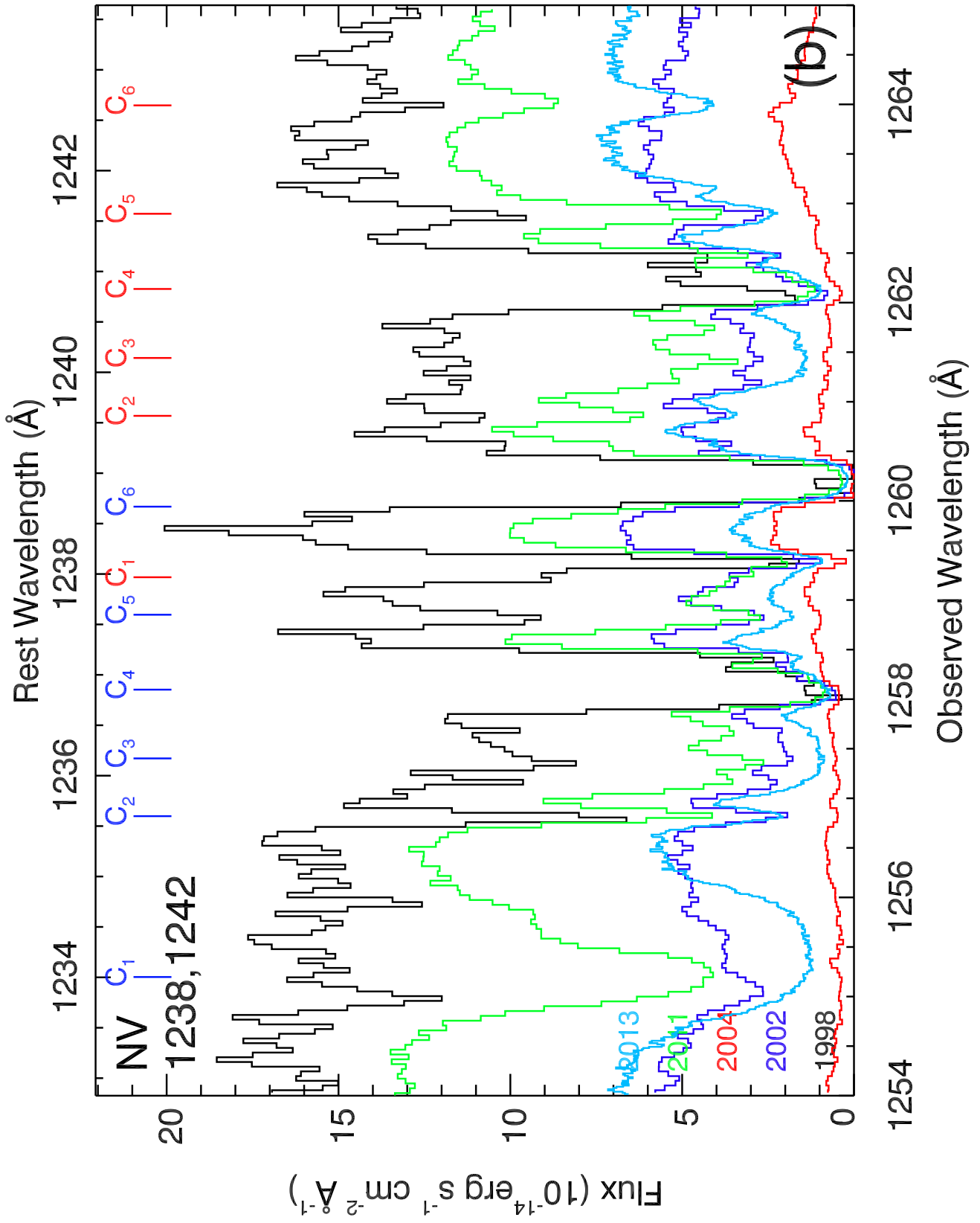


Fig. A.2.b. continued.

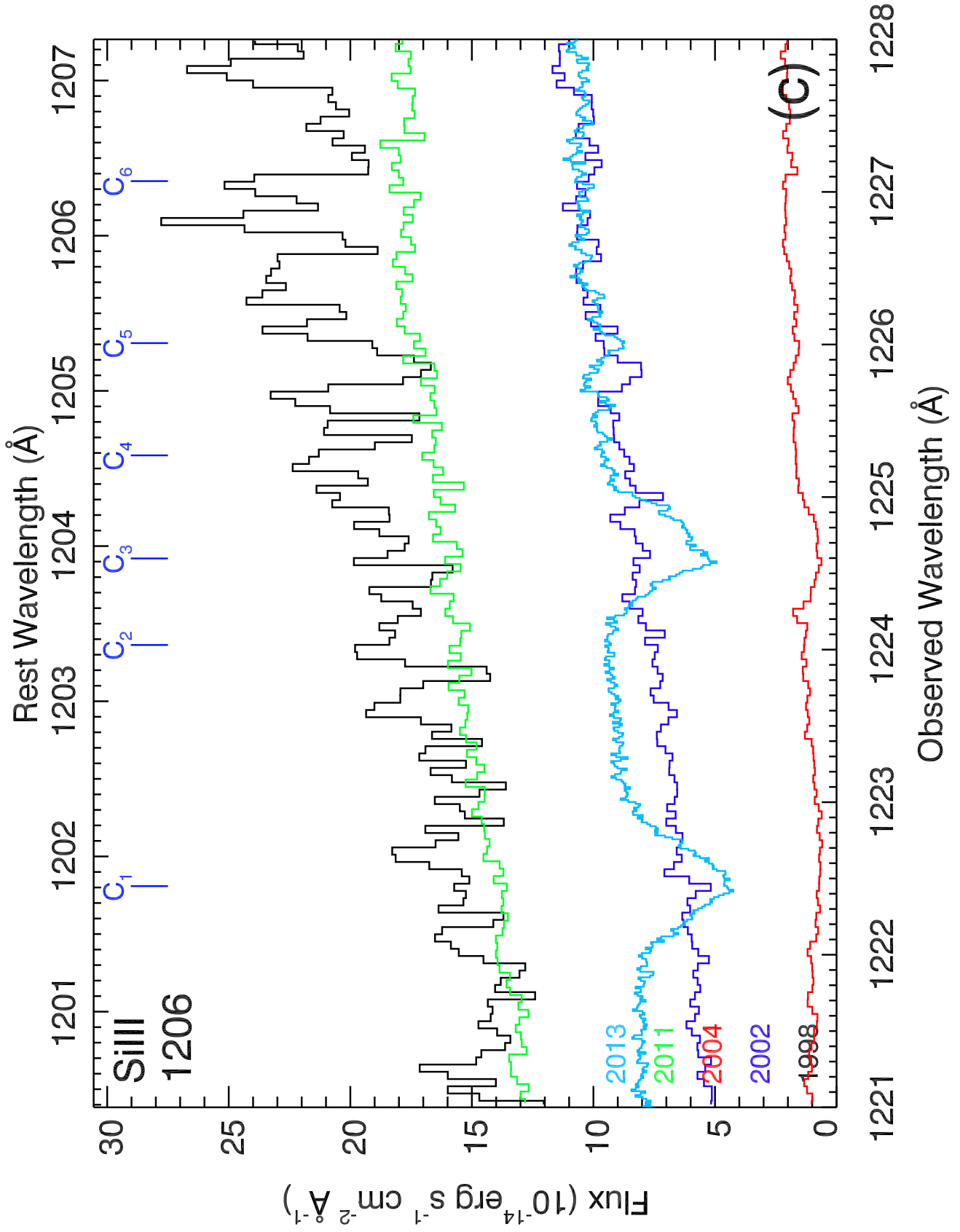


Fig. A.2.c. continued.

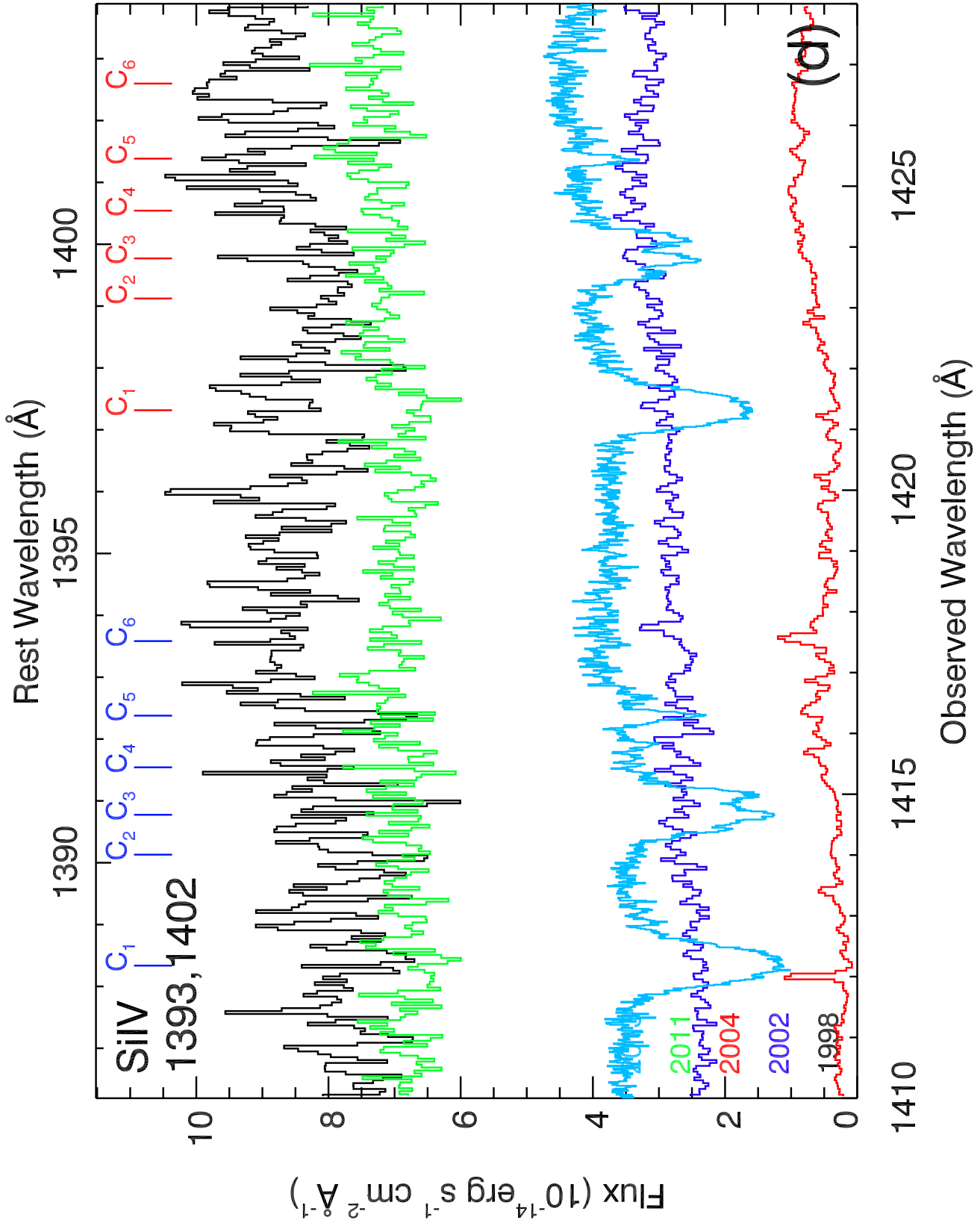


Fig. A.2.d. continued.

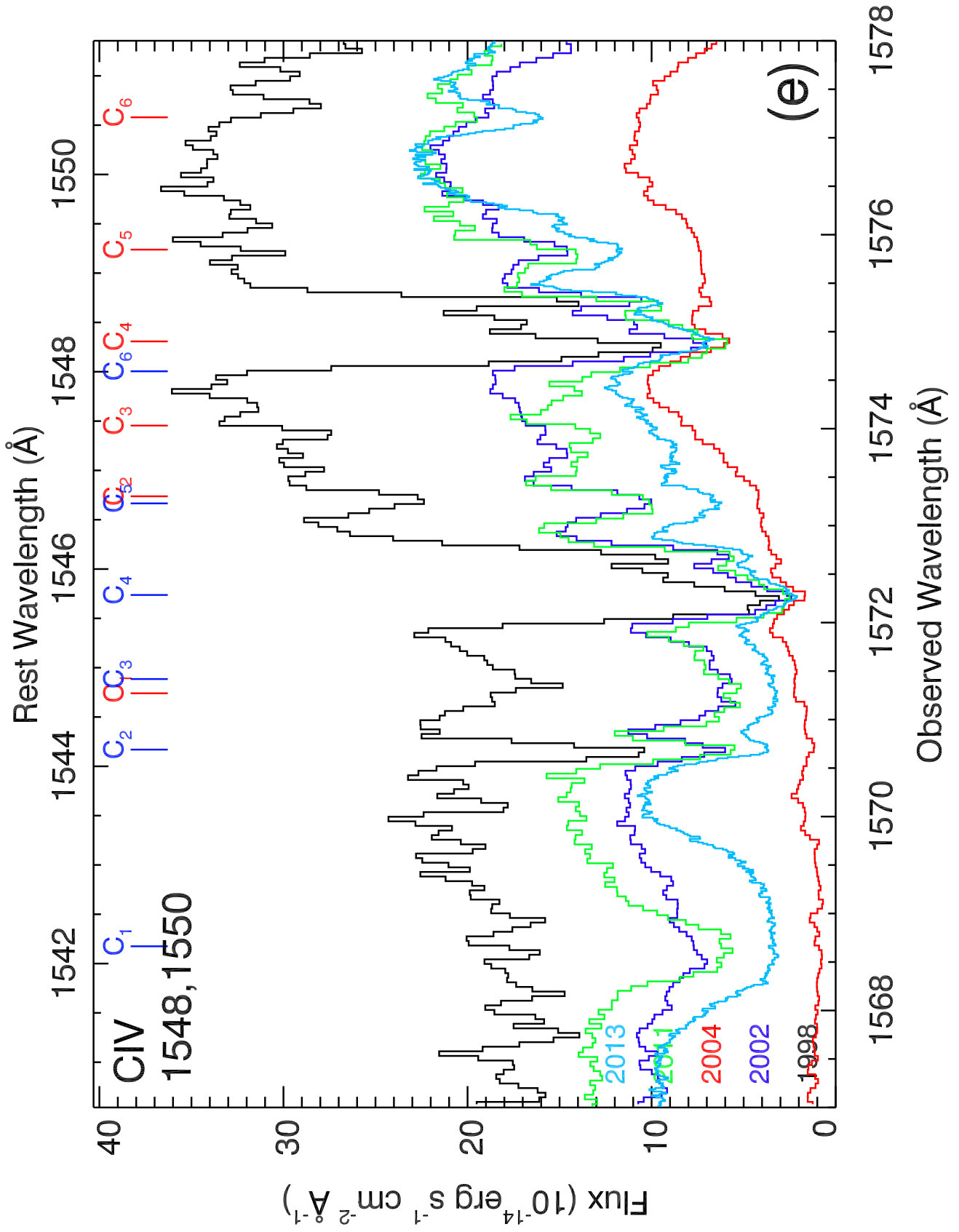


Fig. A.2.e. continued.

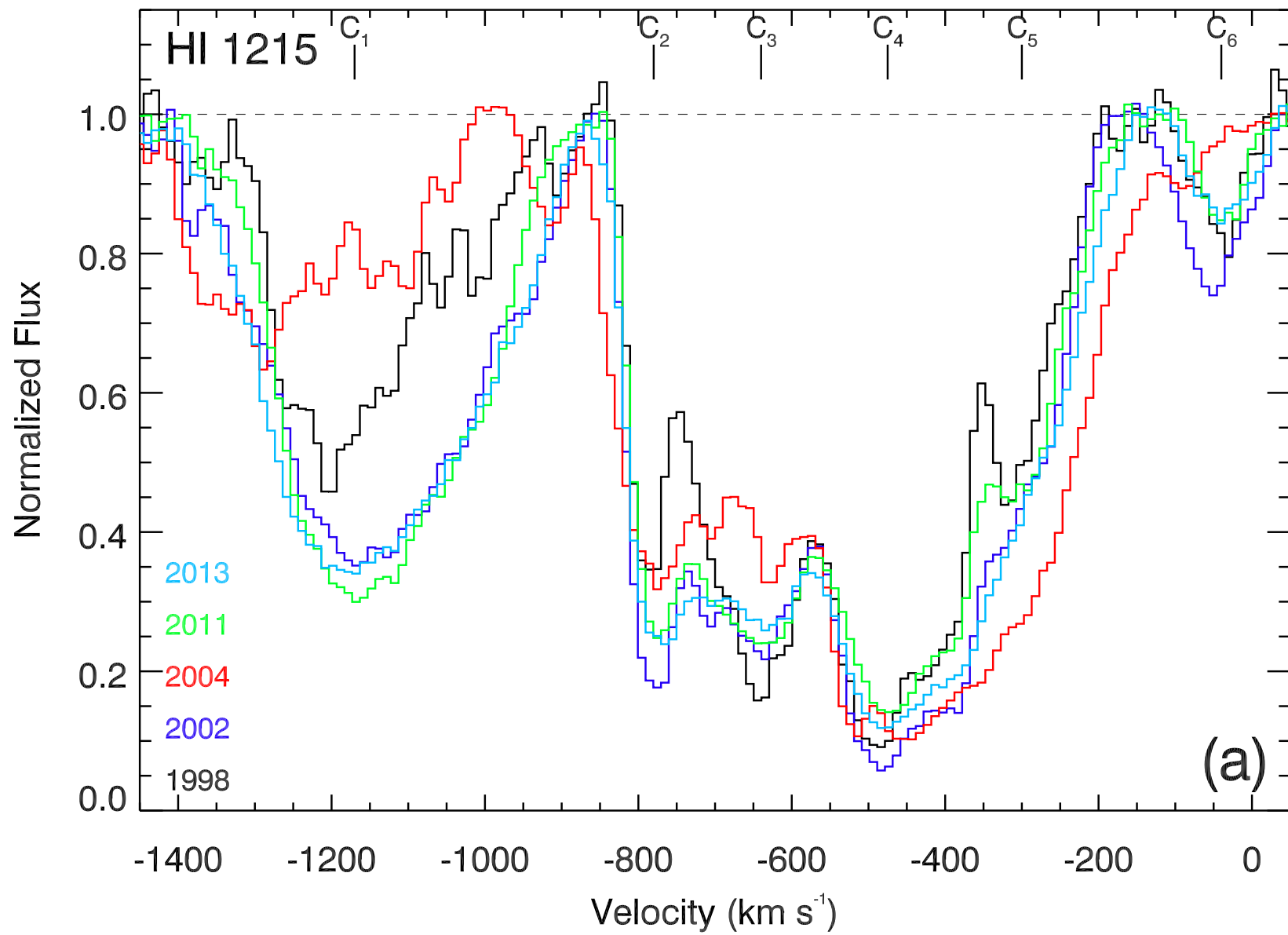


Fig. A.3.a. A plot of the normalized spectrum of NGC 5548 during the five epochs of observation, plotted in the velocity rest-frame of the quasar (same annotation as Fig A.2).

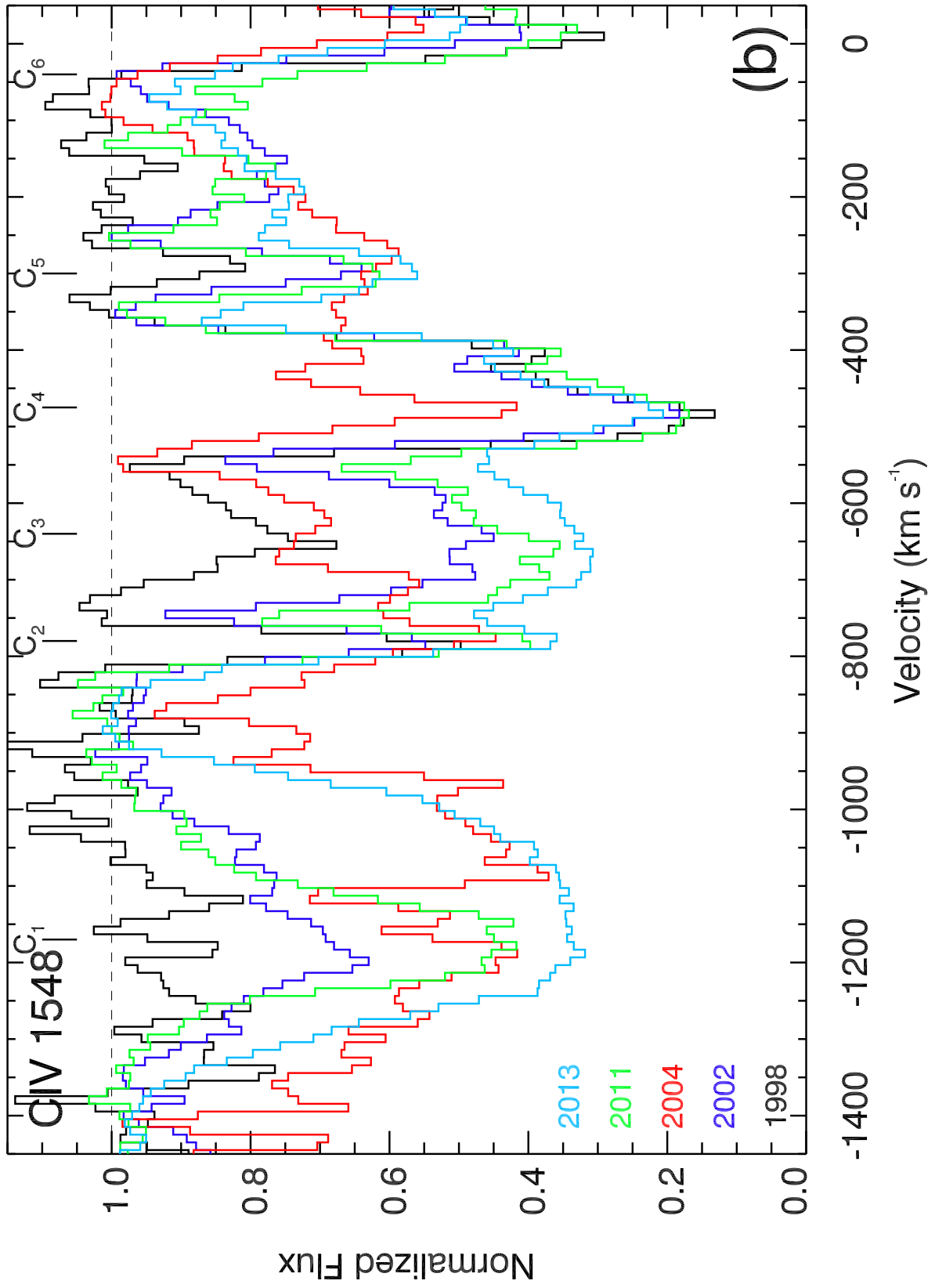


Fig. A.3.b. continued.

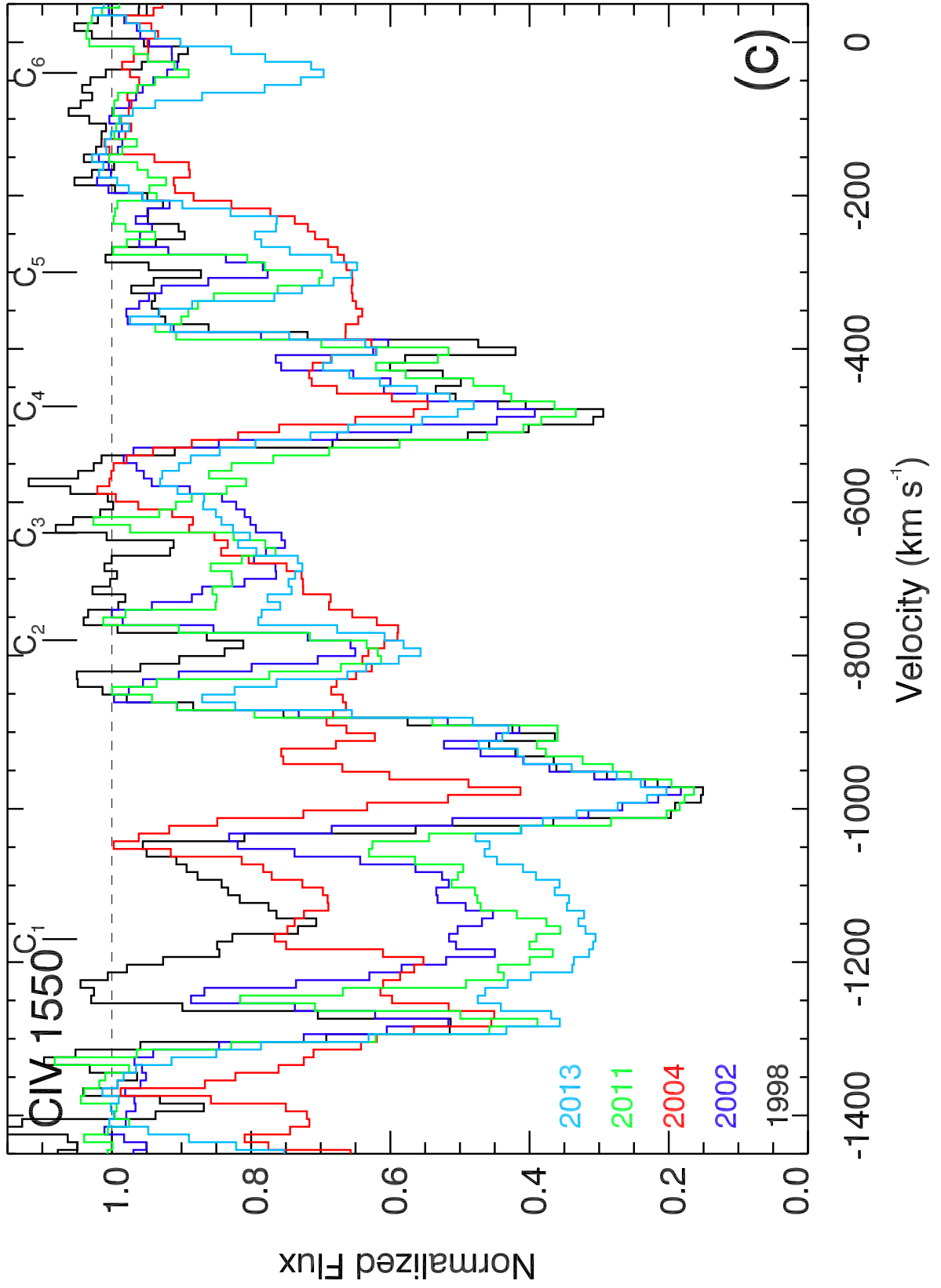


Fig. A.3.c. continued.

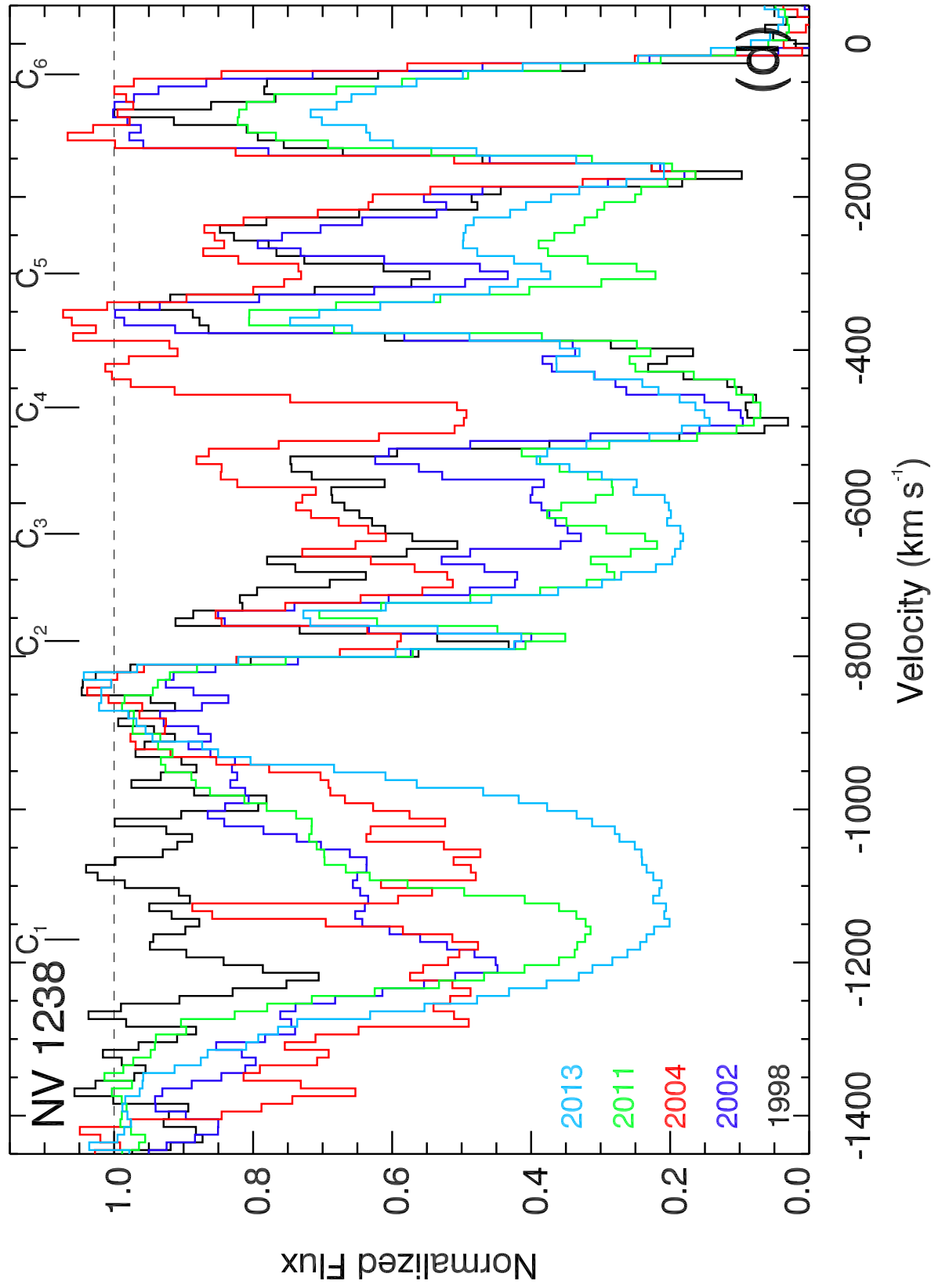


Fig. A.3.d. continued.

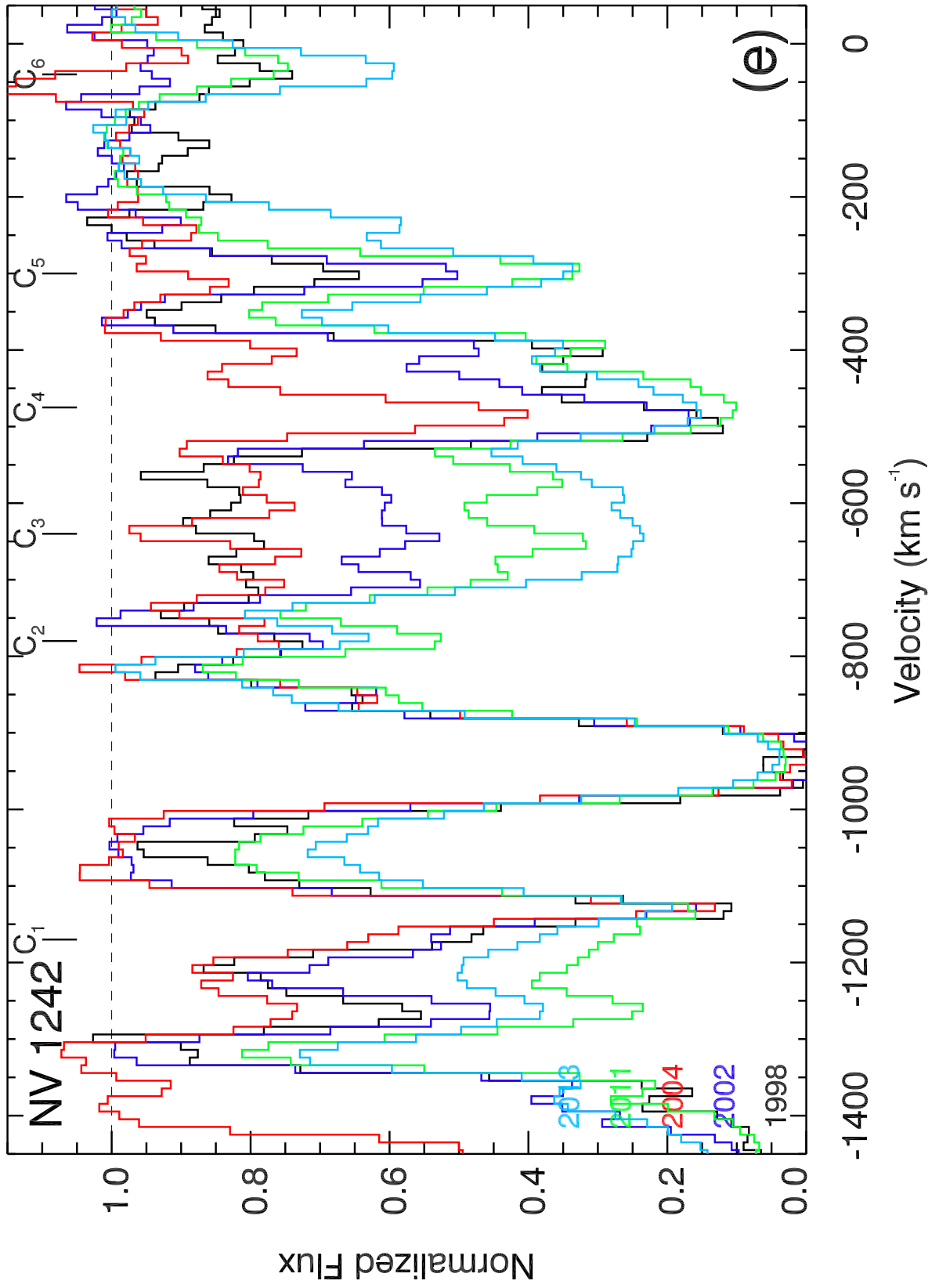


Fig. A.3.e. continued.

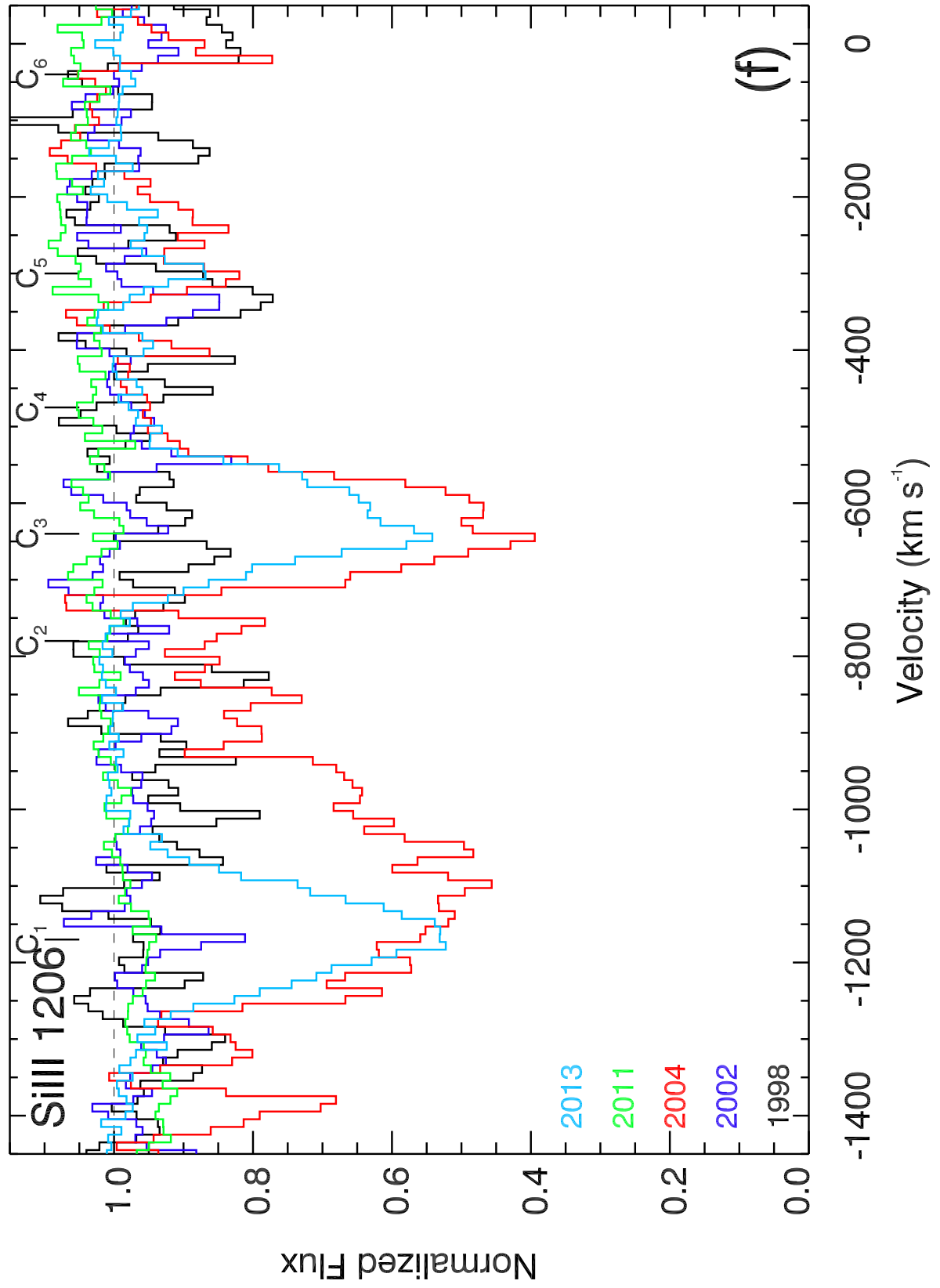


Fig. A.3.f. continued.

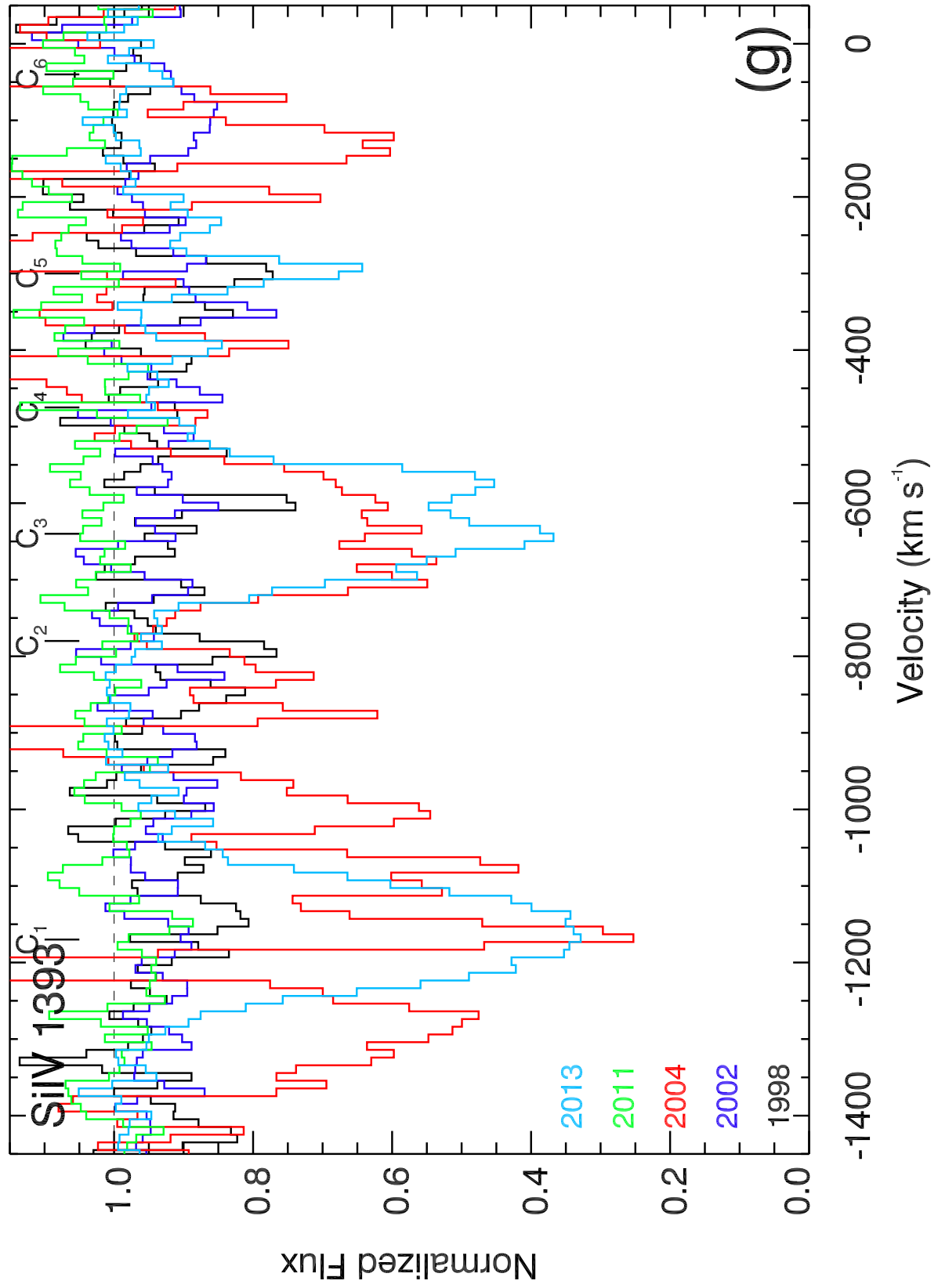


Fig. A.3.g. continued.

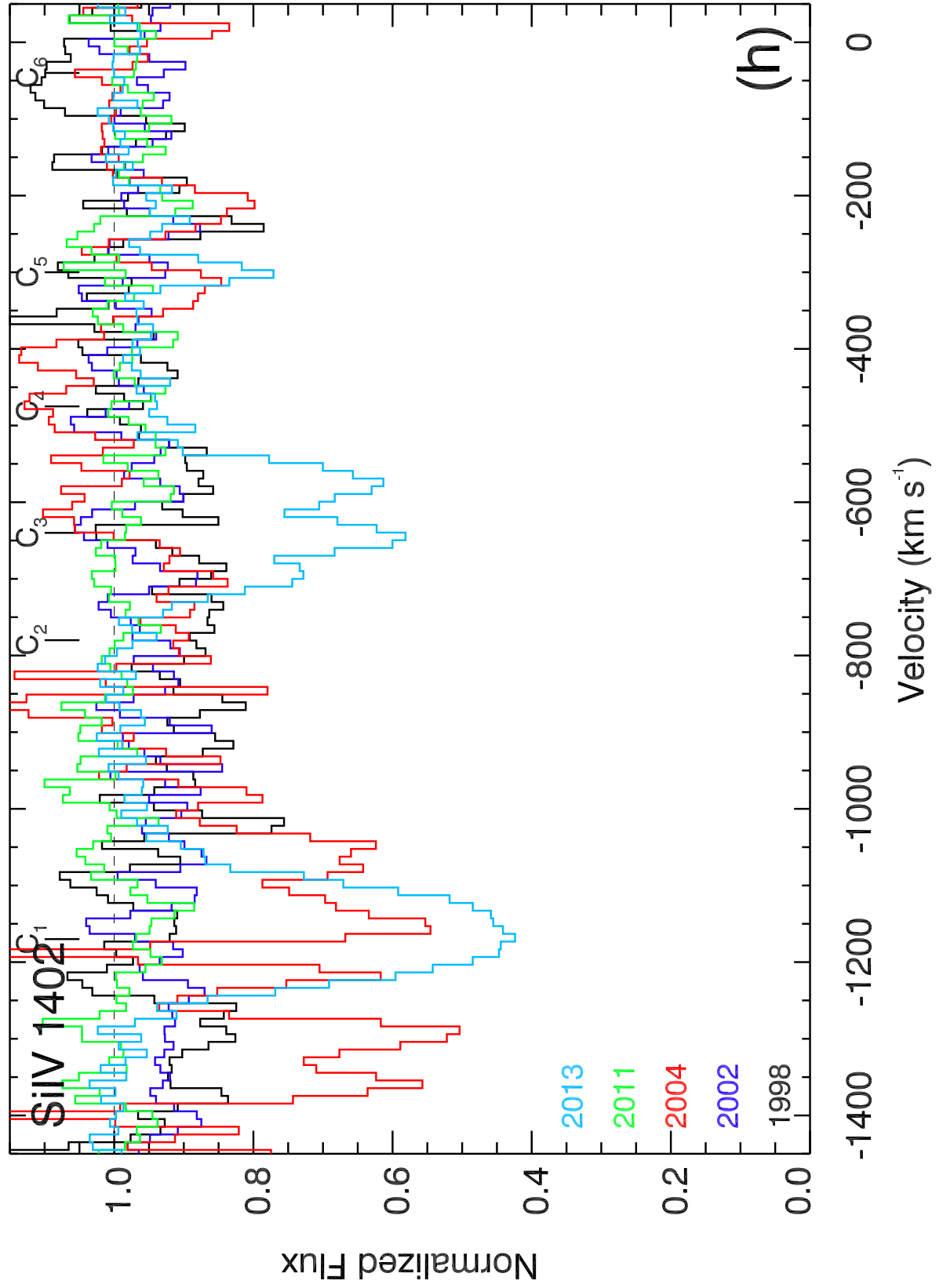


Fig. A.3.h. continued.